The Astrophysical Journal, 843:33 (27pp), 2017 July 1 https://doi.org/10.3847/1538-4357/aa74c8

The SOFIA Massive (SOMA) Star Formation Survey. I. Overview and First Results

James M. De Buizer[1], Mengyao Liu[2], Jonathan C. Tan[2,3,4], Yichen Zhang[5,6], Maria T. Beltrán[7], Ralph Shuping[1], Jan E. Staff[2,8], Kei E. I. Tanaka[2], and Barbara Whitney[9]
[1] SOFIA-USRA, NASA Ames Research Center, MS 232-12, Moffett Field, CA 94035, USA
[2] Department of Astronomy, University of Florida, Gainesville, FL 32611, USA
[3] Department of Physics, University of Florida, Gainesville, FL 32611, USA
[4] National Astronomical Observatory, Mitaka, Tokyo 181-8588, Japan
[5] Departamento de Astronomía, Universidad de Chile, Casilla 36-D, Santiago, Chile
[6] The Institute of Physical and Chemical Research (RIKEN), Hirosawa 2-1, Wako-shi, Saitama 351-0198, Japan
[7] INAF-Osservatorio Astrofisico di Arcetri, Largo E. Fermi 5, I-50125 Firenze, Italy
[8] College of Science and Math, University of Virgin Islands, St. Thomas, VI 00802, USA
[9] Department of Astronomy, University of Wisconsin-Madison, 475 N. Charter St, Madison, WI 53706, USA
Received 2016 October 17; revised 2017 April 1; accepted 2017 April 21; published 2017 June 28

Abstract

We present an overview and first results of the Stratospheric Observatory For Infrared Astronomy Massive (SOMA) Star Formation Survey, which is using the FORCAST instrument to image massive protostars from ∼10 to 40 μm. These wavelengths trace thermal emission from warm dust, which in Core Accretion models mainly emerges from the inner regions of protostellar outflow cavities. Dust in dense core envelopes also imprints characteristic extinction patterns at these wavelengths, causing intensity peaks to shift along the outflow axis and profiles to become more symmetric at longer wavelengths. We present observational results for the first eight protostars in the survey, i.e., multiwavelength images, including some ancillary ground-based mid-infrared (MIR) observations and archival *Spitzer* and *Herschel* data. These images generally show extended MIR/FIR emission along directions consistent with those of known outflows and with shorter wavelength peak flux positions displaced from the protostar along the blueshifted, near-facing sides, thus confirming qualitative predictions of Core Accretion models. We then compile spectral energy distributions and use these to derive protostellar properties by fitting theoretical radiative transfer models. Zhang and Tan models, based on the Turbulent Core Model of McKee and Tan, imply the sources have protostellar masses $m_* \sim 10$–$50\,M_\odot$ accreting at $\sim 10^{-4}$–$10^{-3}\,M_\odot\,\mathrm{yr}^{-1}$ inside cores of initial masses $M_c \sim 30$–$500\,M_\odot$ embedded in clumps with mass surface densities $\Sigma_{\rm cl} \sim 0.1$–$3\,\mathrm{g\,cm}^{-2}$. Fitting the Robitaille et al. models typically leads to slightly higher protostellar masses, but with disk accretion rates ∼100× smaller. We discuss reasons for these differences and overall implications of these first survey results for massive star formation theories.

Key words: dust – infrared: stars – ISM: jets and outflows – stars: early-type – stars: formation – stars: winds, outflows

Supporting material: data behind figures, machine-readable tables

1. Introduction

The enormous radiative and mechanical luminosities of massive stars impact a vast range of scales and processes, from reionization of the universe, to galaxy evolution, to regulation of the interstellar medium, to formation of star clusters, and even to formation of planets around stars in such clusters. Furthermore, synthesis and dispersal of heavy elements by massive stars play key roles in the chemical evolution of the cosmos. In spite of this importance, there is still no consensus on the basic formation mechanism of massive stars. Theories range from Core Accretion models, i.e., scaled-up versions of low-mass star formation (e.g., the Turbulent Core Model of McKee & Tan 2002, 2003; hereafter MT03), to Competitive Accretion models at the crowded centers of forming star clusters (Bonnell et al. 2001; Wang et al. 2010), to Protostellar Collisions (Bonnell et al. 1998; Bally & Zinnecker 2005).

This confusion is due in part to the typically large distances ($\gtrsim$1 kpc) and extinctions to massive protostars (see, e.g., Tan et al. 2014 for a review). Massive stars are observed to form in dense gas clumps with mass surface densities of $\Sigma_{\rm cl} \sim 1\,\mathrm{g\,cm}^{-2}$ (i.e., $A_V \sim 200$ mag; $A_{8\,\mu\mathrm{m}} \sim 8$ mag; $A_{37\,\mu\mathrm{m}} \sim 3$ mag; adopting the opacities of the moderately coagulated thin ice mantle dust model of Ossenkopf & Henning 1994). If massive cores are in approximate pressure and virial equilibrium with this clump (MT03), then such a core with mass M_c has radius $R_c = 0.057\,(\Sigma_{\rm cl}/\mathrm{g\,cm}^{-2})^{-1/2}(M_c/60\,M_\odot)^{1/2}$ pc. If the degree of rotational support is similar to that in low-mass cores, then the disk size should be ∼100–10^3 au in radius (i.e., $\lesssim 1''$ in size for sources at distances of $\gtrsim$1 kpc). The accretion rate is expected to be a few $\times 10^{-4}\,M_\odot\,\mathrm{yr}^{-1}$.

Collimated bipolar outflows are observed from massive protostars (e.g., Beuther et al. 2002) and massive early-stage cores (Tan et al. 2016). These are thought to be accretion powered, driven by rotating magnetic fields that are coupled to the accretion disk and/or the protostar leading to disk winds (e.g., Königl & Pudritz 2000) or X-winds (Shu et al. 2000), respectively. Such protostellar outflows are expected to limit the star formation efficiency from a core to ∼0.5 (Matzner & McKee 2000; Zhang et al. 2014b; hereafter ZTH14; Kuiper et al. 2015), since they expel core material from polar directions.

Creation of low-density outflow cavities is expected to have a profound effect on the mid-infrared (MIR) appearance of massive protostars (De Buizer 2006). Radiative transfer calculations of the MT03 Core Accretion model of massive

protostars (a single protostar in an individual core) have confirmed the importance of these cavities on the MIR to FIR images and spectral energy distributions (SEDs; Zhang & Tan 2011; Zhang et al. 2013b; hereafter ZTM13; ZTH14; Y. Zhang & J. C. Tan 2017, in preparation). Shorter wavelength light tends to emerge along the outflow cavity that is directed toward our line of sight, i.e., the near-facing, blueshifted side of the outflow. At near-infrared (NIR) wavelengths, the appearance of the protostars is typically dominated by scattered light escaping from the cavities. Moving to MIR wavelengths, especially $\gtrsim$10 μm, thermal emission from warm dust in the outflow and outflow cavity walls makes the dominant contribution. The far-facing outflow cavity appears much fainter because of absorption by the dense, colder dusty material in the core envelope. However, as one observes at longer wavelengths (e.g., $\gtrsim$40 μm), the optical depth is reduced, the far-facing outflow cavity becomes more visible, and the appearance of the protostar (i.e., the intensity profile along its outflow axis) becomes more symmetric.

The *Stratospheric Observatory For Infrared Astronomy* (*SOFIA*) FORCAST instrument has the ability to observe from MIR wavelengths up to ~40 μm with $\lesssim$3″ angular resolution. It is thus able to test the above key predictions of Core Accretion models of massive star formation, i.e., their MIR morphologies should be aligned with outflow cavities and that at longer wavelengths the far-facing cavity should become visible as the overall appearance becomes more symmetric. We note that SOFIA's few arcsecond resolution at ~40 μm means that these observations are sensitive to FIR morphologies that are induced by the expected properties of the core infall envelope, rather than by the disk (also, disks in Competitive Accretion models are expected to be even smaller than those in Core Accretion models) and that it is the differences in the predictions of the theoretical formation models on these core envelope scales that can be tested.

We used SOFIA-FORCAST Early Science observations of the massive protostar G35.20–0.74 for such a test of the models (Zhang et al. 2013a). The observations at 37 μm were able to achieve a high dynamic range in flux brightness sensitivity of a factor of $\sim 10^4$ and clearly detected the fainter far-facing outflow cavity at both 31 and 37 μm. Detailed modeling of the multiwavelength intensity profiles along the outflow axis, together with the SED, provided the following constraints on the properties of the massive protostar, assuming it is the single dominant source of luminosity: a current stellar mass of $m_* \sim 20$–$34\,M_\odot$, embedded in a core with $M_c = 240\,M_\odot$, in a clump with $\Sigma_{\rm cl} \simeq 0.4$–$1\ {\rm g\ cm^{-2}}$.

This work has motivated observations of a larger sample of protostars, i.e., the SOFIA Massive (SOMA) Star Formation Survey (PI: Tan). The goal is to observe at least ~50 protostars spanning a range of environments, evolutionary stages, and core masses. We have defined four types of sources: Type I: "MIR sources in IRDCs"—relatively isolated sources in Infrared Dark Clouds, some without detected radio emission; Type II: "Hyper-compact"—often jet-like, radio sources, where the MIR emission extends beyond the observed radio emission (e.g., G35.20–0.74); Type III: "Ultra-compact"—radio sources where the radio emission is more extended than the MIR emission; Type IV: "Clustered sources"—an MIR source exhibiting radio emission is surrounded by several other MIR sources within ~60″. Such classification is somewhat arbitrary, e.g., depending on the sensitivity of the MIR or radio continuum observations, but an evolutionary sequence is expected to hold from Types I to III. A theoretical calculation of the radio continuum emission from the early phases of ionization, i.e., of a disk wind outflow, has been presented by Tanaka et al. (2016).

Source selection for the SOMA survey mainly utilized the CORNISH survey of centimeter continuum emission (Hoare et al. 2012), complemented by radio-quiet MIR sources in IRDCs studied by Butler & Tan (2012) and protostars studied at 24 μm by de Wit et al. (2009). We included some non-Galactic plane sources and attempted, where possible, to have a relatively spread-out distribution on the sky, which aids in the scheduling of SOFIA observations.

In this first paper of the SOMA survey, we present the results of the first eight sources (including G35.20–0.74), which were observed up to the end of 2014. These are all Type II sources. Our goal here is to present the survey data, including public release of the calibrated images, of these eight sources. We will use these sources to further test the hypothesis that the appearance of the MIR morphologies of massive young stellar objects (MYSOs) may be influenced by outflows. We will also measure the SEDs of the sources and derive fitting solutions from radiative transfer models, especially the Zhang−Tan et al. series (hereafter the ZT models) that were specifically developed for massive protostars. We will also compare the results of fitting with the more general, commonly used Robitaille et al. (2007) radiative transfer models. Future papers will carry out more detailed analyses of images, including outflow axis intensity profiles, as well as presenting data for additional sources.

2. Observations

2.1. SOFIA Data

The following eight sources, AFGL 4029, AFGL 437, IRAS 07299–1651, G35.20–0.74, G45.45+0.05, IRAS 20126+4104, Cepheus A, and NGC 7538 IRS9, were observed by SOFIA[10] (Young et al. 2012) with the FORCAST instrument (Herter et al. 2013; see Table 1). Data were taken on multiple flights spanning the Early Science period, Cycle 1, and Cycle 2 SOFIA observing cycles, though typically a single target was observed to completion on a single flight. All observations were taken at an altitude between 39,000 and 43,000 ft, which typically yields precipitable water vapor overburdens of less than 25 μm.

FORCAST is a facility imager and spectrograph that employs a Si:As 256 × 256 blocked-impurity band (BIB) detector array to cover a wavelength range of 5–25 μm and a Si:Sb 256 × 256 BIB array to cover the range from 25 to 40 μm. FORCAST has a dichroic that allows simultaneous imaging with both arrays, if desired. In imaging mode, the arrays cover a 3.′4 × 3.′2 instantaneous field of view with $0.''768^2$ pixels (after distortion correction). All data were taken by employing the standard chop−nod observing technique used in the thermal infrared, with chop and nod throws sufficiently large to sample clear off-source sky.

G35.20–0.74 was observed in the Early Science phase of SOFIA and was imaged in three filters: 19 μm ($\lambda_{\rm eff} = 19.7$ μm; $\Delta\lambda = 5.5$ μm), 31 μm ($\lambda_{\rm eff} = 31.5$ μm; $\Delta\lambda = 5.7$ μm), and 37 μm ($\lambda_{\rm eff} = 37.1$ μm; $\Delta\lambda = 3.3$ μm). Observations of the rest of the targets presented here were taken in four filters. For

[10] SOFIA is jointly operated by the Universities Space Research Association, Inc. (USRA), under NASA contract NAS2-97001, and the Deutsches SOFIA Institut (DSI) under DLR contract 50 OK 0901 to the University of Stuttgart.

Table 1
SOFIA-FORCAST Observations: Observation Dates and Exposure Times (s)

Source	R.A.(J2000)	Decl.(J2000)	d (kpc)	Obs. Date	7.7 μm	11.1 μm	19.7 μm	25.3 μm	31.5 μm	37.1 μm
AFGL 4029	$03^h01^m31\overset{s}{.}28$	$+60°29'12\overset{''}{.}87$	2.0	2014 Mar 29	112	…	158	…	282	678
AFGL 437	$03^h07^m24\overset{s}{.}55$	$+58°30'52\overset{''}{.}76$	2.0	2014 Jun 11	217	…	2075	…	2000	884
IRAS 07299–1651	$07^h32^m09\overset{s}{.}74$	$-16°58'11\overset{''}{.}28$	1.68	2015 Feb 06	280	…	697	…	449	1197
G35.20–0.74	$18^h58^m13\overset{s}{.}02$	$+01°40'36\overset{''}{.}2$	2.2	2011 May 25	…	909	959	…	4068	4801
G45.47+0.05	$19^h14^m25\overset{s}{.}67$	$+11°09'25\overset{''}{.}45$	8.4	2013 Jun 26	…	309	…	588	316	585
IRAS 20126+4104	$20^h14^m26\overset{s}{.}05$	$+41°13'32\overset{''}{.}48$	1.64	2013 Sep 13	…	484	…	1276	487	1317
Cepheus A	$22^h56^m17\overset{s}{.}98$	$+62°01'49\overset{''}{.}39$	0.70	2014 Mar 25	242	…	214	…	214	1321
NGC 7538 IRS9	$23^h14^m01\overset{s}{.}77$	$+61°27'19\overset{''}{.}8$	2.65	2014 Jun 06	215	…	653	…	491	923

(This table is available in machine-readable form.)

targets observed early in Cycle 1, namely G45.47+0.05 and IRAS 20126+4104, the SOFIA 11 μm ($\lambda_{\rm eff} = 11.1$ μm; $\Delta\lambda = 0.95$ μm) and 25 μm ($\lambda_{\rm eff} = 25.3$ μm; $\Delta\lambda = 1.86$ μm) filters were employed in the short wavelength camera of FORCAST. After Cycle 1, it was determined that it would be better to use the 7 μm ($\lambda_{\rm eff} = 7.7$ μm; $\Delta\lambda = 0.47$ μm) instead of the 11 μm filter because it is closer in wavelength to the *Spitzer* 8 μm filter, which we could use to derive accurate absolute calibration from the *Spitzer* data. At the same time we decided to use the 19 μm filter instead of the 25 μm filter because it is broader and offers better sensitivity. The two filters used in the long wavelength camera, 31 and 37 μm, were used for all Cycle 1 and 2 sources in the survey.

SOFIA data were calibrated by the SOFIA pipeline with a system of stellar calibrators taken across all flights in a flight series and applied to all targets within that flight series (see also the FORCAST calibration paper by Herter et al. 2013). Corrections are made for the airmass of the science targets as well. The main source of uncertainty in the SOFIA calibrations is the variability observed in the standard stars' observed flux throughout the flight and from flight to flight due to changing atmospheric conditions. The standard deviation of these measurements will be used as our 1σ error on the quoted flux density measurements, and these are: 2.9% at 7 μm, 1.0% at 11 μm, 3.1% at 19 μm, 5.1% and 25 μm, 3.6% at 31 μm, and 4.6% at 37 μm.

2.2. Spitzer and Herschel Archival Data

For all objects, data were retrieved from the *Spitzer* Heritage Archive from all four IRAC (Fazio et al. 2004) channels (3.6, 4.5, 5.8 and 8.0 μm). In many cases, the sources in this sample were so bright that they are saturated in the IRAC images and could not be used to derive accurate fluxes. Additionally, we incorporated publicly available imaging observations performed with the *Herschel Space Observatory*[11] (Pilbratt et al. 2010) and its PACS (Poglitsch et al. 2010) and SPIRE (Griffin et al. 2010) instruments at 70, 160, 250, 350, and 500 μm. The exception is IRAS 07229-6151, for which no *Herschel* data exist.

[11] *Herschel* is an ESA space observatory with science instruments provided by European-led Principal Investigator consortia and with important participation from NASA. The *Herschel* data used in this paper are taken from the Level 2 (flux-calibrated) images provided by the *Herschel* Science Center via the NASA/IPAC Infrared Science Archive (IRSA), which is operated by the Jet Propulsion Laboratory, California Institute of Technology, under contract with NASA.

In addition to using these data for deriving multiwavelength flux densities of our sources, the *Spitzer* 8 μm and *Herschel* 70 μm images are presented for comparison with our SOFIA images in Section 4.1.

The *Herschel* images, particularly at 70 μm, can suffer from relatively poor image quality due to observations being taken in fast scanning mode. Point sources are often not circularly symmetric, and can be severely triangular or square. To enable comparative morphology as a function of wavelength, the *Herschel* 70 μm images were deconvolved to remove most of this asymmetry and to improve the resolution to be more comparable to the resolution of SOFIA at 37 μm.

2.3. Data Resolutions and Deconvolutions

The resolution of SOFIA through the FORCAST wavelength range is only slightly dependent upon the effective filter central wavelength. This is because the image quality is dominated by in-flight telescope pointing stability, at least at the shorter wavelengths of FORCAST. The typical resolution achieved for filters with effective central wavelengths $\lesssim$25 μm was about 3″. At wavelengths $\gtrsim$20 μm, it appears that we are observing near the diffraction limit. Thus, resolutions presented in the *Spitzer* and SOFIA images in Section 4.1 are fairly similar, i.e., 2.″0 for the *Spitzer* 8 μm images, 2.″7 at SOFIA 7 μm, 2.″9 at SOFIA 11 μm, 3.″3 at SOFIA 19 and 25 μm, 3.″4 at 31 μm, and 3.″5 at 37 μm.

As discussed above, the *Herschel* 70 μm images were deconvolved to improve image quality and resolution. Deconvolution techniques employ an iterative approach, where the greater the number of iterations, the better the effective resolution. However, iterating too much can create artifacts and false structure in the final deconvolved images. We employed a maximum likelihood approach, using the max_likelihood.pro script written by F. Varosi and available in the public IDL astronomy program database (http://idlastro.gsfc.nasa.gov). We mildly deconvolved the images (employing no more than 30 iterations), which tends to correct image PSF abnormalities and create images with effective resolutions a factor of 1.5–2.0 better than the native image resolution. Proper deconvolutions require an accurate representation of the image PSF. Therefore, for each source in our survey, the rest of the *Herschel* image field was scoured for point sources and a median combination of all these point sources (after normalization) was created and used in the deconvolution. The resultant images have resolutions of 5.″0–5.″2, which is ~1.6 times better than the measured 8.″1 native resolution of *Herschel* at 70 μm.

2.4. Astrometry

SOFIA observations were performed using the simultaneous observations with the dichroic in such a way that the relative astrometry between the four SOFIA images has been determined to be better than a FORCAST pixel (~0.″77). The absolute astrometry of the SOFIA data comes from matching the morphology at the shortest SOFIA wavelength (either 7 or 11 μm) with the *Spitzer* 8 μm image (or shorter IRAC wavelength, if saturated at 8 μm). The *Herschel* 70 μm data were found to be off in their absolute astrometry by up to 5″. For all targets in this survey, we were able to find multiple sources in common between the 70 μm *Herschel* image and sources found in the SOFIA or *Spitzer* field of view that allowed us to correct the *Herschel* 70 μm absolute astrometry, which is then assumed to have errors of less than 1″.

2.5. Other Ground-based IR Data

Published and unpublished data from other facilities were also available for a few sources in our survey and were incorporated into the SEDs and model fitting (see Table 2). For G35.20–0.74, 11.7 μm (*Si-5*) and 18.3 μm (*Qa*) data from the Gemini Observatory T-ReCS instrument (De Buizer & Fisher 2005) were first published in De Buizer (2006). For IRAS 20126+4104, Gemini T-ReCS 12.5 μm (*Si-6*) and 18.3 μm data were also previously published in De Buizer (2007). There are also previously unpublished Gemini T-ReCS 11.7 and 18.3 μm data for IRAS 07299–1651 that we present here. For G45.47+0.05, we have on hand previously unpublished imaging data from the NASA/Infrared Telescope Facility (IRTF) at *K* and *L* from the NSFCam instrument (Shure et al. 1994), as well as previously published (De Buizer et al. 2005) 11.7 μm (*N4*) and 20.8 μm (*Q3*) data from the MIR camera MIRLIN (Ressler et al. 1994).

3. Analysis Methods

3.1. Derivation of Spectral Energy Distributions

We build SEDs of the eight sources from 3.6 μm up to 500 μm with photometric data from *Spitzer*, IRTF, Gemini, SOFIA and *Herschel*. The uncertainties are mainly systematic, arising from calibration, which is in general about 10%. We used PHOTUTILS, a Python package to measure the flux photometry.

The position of the protostellar source is generally fixed from published literature results, e.g., radio continuum emission peak that is located along a known outflow axis (see Section 4.1). Bright free–free emission can arise from externally ionized dense clumps, so ideally confirmation of protostellar location should also be obtained from high-resolution studies of tracers of hot cores (i.e., warm, dense gas) and outflows. However, as we discuss in Section 4.1, typically we do not consider that there are large uncertainties in the source location.

Then, circular apertures of radius $R_{\rm ap}$ are chosen to cover most of the emission. We try two methods: (1) Fixed Aperture Radius—the radius is set by considering the morphology of the *Herschel* 70 μm image[12] so as to include most of the source flux while minimizing contamination from neighboring sources and (2) Variable Aperture Radius—the radii at wavelengths <70 μm are varied based on the morphology at each wavelength, again aiming to minimize contamination from neighboring sources.

The emission at the longer *Herschel* wavelengths ($\geqslant$160 μm) is typically more extended, which is both a real effect of the presence of a cooler, massive clump surrounding the protostars, and also a result of the lower resolution of these data. This is the main motivation for us to then carry out background subtraction of the fluxes, based on the median flux density in an annular region extending from 1 to 2 aperture radii.

Summarizing, for wavelengths $\leqslant$70 μm, the aperture radii are typically at least several times larger than the beam sizes (and by greater factors for the fixed aperture method that uses the 70 μm aperture radii across all bands). At longer wavelengths, where the fixed aperture radius set at 70 μm is always used, the aperture diameter in a few sources (AFGL 4029, G45.47+0.05, IRAS 20126) begins to become similar to the image resolutions at the longest wavelengths, i.e., toward 500 μm. However, as we will see, for the wavelengths defining the peak of the SEDs, the source apertures are always significantly larger than the image resolutions.

3.2. SED Models and Fitting

3.2.1. Zhang & Tan (ZT) Models

In a series of papers, Zhang & Tan (2011), Zhang et al. (2013b), ZTH14, and Y. Zhang & J. C. Tan (2017, in preparation) have developed models for the evolution of high- and intermediate-mass protostars based on the Turbulent Core model (MT03). Zhang & Tan (2015) extended these models to treat lower-mass protostars. For massive star formation, the initial conditions are pressurized, dense, massive cores embedded in high mass surface density "clump" environments. The initial conditions are parameterized by the initial core mass (M_c) and the mean mass surface density of the clump environment ($\Sigma_{\rm cl}$). The latter affects the surface pressure on the core and therefore, together with M_c, determines their sizes and densities. Cores undergo inside-out collapse (Shu 1977; McLaughlin & Pudritz 1996, 1997) with the effect of rotation described with the solution by Ulrich (1976).

Massive disks are expected to form around massive protostars due to the high accretion rates. We assume that the mass ratio between the disk and the protostar is a constant $f_d = m_d/m_* = 1/3$, considering the rise in effective viscosity due to disk self-gravity at about this value of f_d (Kratter et al. 2008). The disk size is calculated from the rotating collapse of the core (ZTH14), with the rotational-to-gravitational energy ratio of the initial core β_c set to be 0.02, which is a typical value from observations of low- and high-mass prestellar cores (e.g., Goodman et al. 1993; Li et al. 2012; Palau et al. 2013). The disk structure is described with an "α-disk" solution (Shakura & Sunyaev 1973), with an improved treatment to include the effects of the outflow and the accretion infall to the disk (ZTM13).

Half of the accretion energy is released when the accretion flow reaches the stellar surface, i.e., the boundary layer luminosity $L_{\rm acc} = Gm_*\dot{m}_*/(2r_*)$, but we assume this part of luminosity is radiated along with the internal stellar luminosity isotropically as a single blackbody with total $L_{*,\rm acc} = L_* + L_{\rm acc}$. This choice is made given the uncertain accretion geometry near the star, e.g., whether accretion streamlines are affected by the stellar magnetic field or if the accretion disk extends all the way in to the stellar surface, and

[12] For IRAS 07299, we adopt the aperture size based on SOFIA 37 μm data since no *Herschel* data are available.

Table 2
Integrated Flux Densities

Facility	λ (μm)	$F_{\lambda,\mathrm{fix}}$[a] (Jy)	$F_{\lambda,\mathrm{var}}$[b] (Jy)	R_{ap}[c] ($''$)	$F_{\lambda,\mathrm{fix}}$ (Jy)	$F_{\lambda,\mathrm{var}}$ (Jy)	R_{ap} ($''$)	$F_{\lambda,\mathrm{fix}}$ (Jy)	$F_{\lambda,\mathrm{var}}$ (Jy)	R_{ap} ($''$)	$F_{\lambda,\mathrm{fix}}$ (Jy)	$F_{\lambda,\mathrm{var}}$ (Jy)	R_{ap} ($''$)	$F_{\lambda,\mathrm{fix}}$ (Jy)	$F_{\lambda,\mathrm{var}}$ (Jy)	R_{ap} ($''$)	$F_{\lambda,\mathrm{fix}}$ (Jy)	$F_{\lambda,\mathrm{var}}$ (Jy)	R_{ap} ($''$)	$F_{\lambda,\mathrm{fix}}$ (Jy)	$F_{\lambda,\mathrm{var}}$ (Jy)	R_{ap} ($''$)	$F_{\lambda,\mathrm{fix}}$ (Jy)	$F_{\lambda,\mathrm{var}}$ (Jy)	R_{ap} ($''$)
		AFGL 4029			AFGL 437			IRAS 07299			G35.20–0.74			G45.47+0.05			IRAS 20126			Cep A			NGC 7538 IRS9		
IRTF/NSFCam	2.1	…	…	…	…	…	…	…	…	…	…	…	…	0.02 (0.08)	0.02 (0.03)	7.7	…	…	…	…	…	…	…	…	…
Spitzer/IRAC	3.6	2.60 (2.71)	2.14 (2.23)	4.8	2.26 (2.39)	1.36 (1.49)	12.0	1.34 (1.42)	1.19 (1.28)	6.0	0.50 (0.60)	0.30 (0.34)	14.0	…	…	…	0.68 (0.73)	0.24 (0.28)	4.8	15.87 (16.51)	6.72 (7.09)	15.0	2.80 (2.99)	2.15 (2.24)	6.0
IRTF/NSFCam	3.8	…	…	…	…	…	…	…	…	…	…	…	…	0.12 (0.08)	0.08 (0.08)	7.7	…	…	…	…	…	…	…	…	…
Spitzer/IRAC	4.5	3.62 (3.75)	2.82 (2.96)	3.6	2.77 (2.87)	1.89 (2.00)	12.0	2.41 (2.54)	2.18 (2.33)	6.0	1.24 (1.24)	0.90 (0.95)	14.0	0.25 (0.35)	0.18 (0.22)	7.7	…	…	…	27.90 (28.67)	13.89 (14.65)	15.0	7.89 (8.15)	5.69 (5.99)	6.0
Spitzer/IRAC	5.8	7.13 (7.63)	6.54 (6.86)	7.2	10.27 (11.05)	5.52 (6.19)	12.0	2.96 (3.15)	2.53 (2.71)	6.0	1.84 (2.64)	1.43 (1.65)	14.0	…	…	…	1.90 (2.24)	0.76 (0.92)	4.8	27.61 (30.11)	13.51 (14.78)	15.0	39.55 (41.17)	31.41 (32.14)	6.0
SOFIA/FORCAST	7.7	12.88 (12.72)	12.22 (12.28)	7.7	29.60 (28.96)	17.04 (18.58)	11.5	3.48 (3.31)	3.48 (3.31)	7.7	…	…	…	…	…	…	…	…	…	21.25 (19.00)	11.08 (12.02)	15.0	64.24 (62.75)	59.12 (59.89)	6.1
Spitzer/IRAC	8.0	10.34 (11.08)	8.86 (9.43)	7.2	24.98 (27.03)	13.38 (15.01)	12.0	2.30 (2.51)	2.12 (2.29)	6.0	3.22 (4.90)	2.85 (3.22)	14.0	0.15 (0.13)	0.14 (0.14)	7.7	1.36 (2.04)	0.44 (0.64)	4.5	13.80 (17.40)	6.52 (7.38)	15.0	41.64 (44.25)	27.49 (29.06)	6.0
IRTF/OSCIR	10.5	…	…	…	…	…	…	…	…	…	…	…	…	2.37 (0.38)	0.07 (0.24)	7.7	…	…	…	…	…	…	…	…	…
SOFIA/FORCAST	11.1	…	…	…	…	…	…	…	…	…	…	…	…	0.36 (0.21)	0.02 (0.05)	7.7	0.41 (0.42)	0.21 (0.26)	3.2	…	…	…	…	…	…
Gemini/T-ReCS	11.7	…	…	…	…	…	…	1.56 (1.71)	1.62 (1.66)	1.8	nan (3.82)	2.14 (2.31)	5.0	0.32 (0.14)	0.36 (0.36)	5.0	…	…	…	…	…	…	…	…	…
Gemini/T-ReCS	12.5	…	…	…	…	…	…	…	…	…	…	…	…	…	…	…	1.87 (1.87)	1.67 (1.69)	6.4	…	…	…	…	…	…
Gemini/T-ReCS	18.3	…	…	…	…	…	…	…	…	…	nan (63.03)	44.96 (48.00)	7.0	2.29 (2.56)	4.92 (4.85)	5.0	23.84 (23.84)	24.12 (24.12)	6.4	…	…	…	…	…	…
SOFIA/FORCAST	19.7	57.25 (59.43)	54.59 (56.22)	7.7	271 (269)	217 (2219)	11.5	73.82 (74.04)	73.82 (74.04)	7.7	68.18 (55.91)	64.87 (63.46)	14.0	…	…	…	…	…	…	138 (132)	179 (167)	24.0	172 (168)	152 (154)	6.1
IRTF/MIRLIN	20.8	…	…	…	…	…	…	…	…	…	…	…	…	5.14 (6.57)	8.78 (8.79)	7.7	…	…	…	…	…	…	…	…	…
SOFIA/FORCAST	25.3	…	…	…	…	…	…	…	…	…	…	…	…	45.98 (33.75)	45.89 (42.18)	7.7	188 (190)	159 (163)	6.4	…	…	…	…	…	…
SOFIA/FORCAST	31.5	187 (194)	171 (178)	7.7	732 (726)	656 (665)	15.4	446 (458)	446 (458)	7.7	553 (551)	502 (512)	14.0	144 (138)	135 (134)	7.7	438 (440)	352 (365)	6.4	2771 (2726)	2453 (2466)	24.0	616 (620)	520 (534)	7.7
SOFIA/FORCAST	37.1	405 (419)	352 (371)	7.7	878 (878)	769 (783)	15.4	681 (705)	681 (705)	7.7	1193 (1120)	1061 (1071)	14.0	214 (202)	189 (189)	7.7	729 (739)	528 (561)	6.4	6262 (6275)	5362 (5451)	24.0	843 (837)	679 (699)	7.7
Herschel/PACS	70.0	350 (394)	350 (394)	11.2	1132 (1181)	1132 (1181)	32.0	…	…	…	2628 (2733)	2628 (2733)	32.0	938 (1093)	938 (1093)	14.4	1398 (1519)	1398 (1519)	12.8	14637 (15298)	14637 (15298)	48.0	1568 (1681)	1568 (1681)	25.6

Table 2
(Continued)

Facility	λ (μm)	$F_{\lambda,\mathrm{fix}}$[a] (Jy)	$F_{\lambda,\mathrm{var}}$[b] (Jy)	R_{ap}[c] (″)	$F_{\lambda,\mathrm{fix}}$ (Jy)	$F_{\lambda,\mathrm{var}}$ (Jy)	R_{ap} (″)	$F_{\lambda,\mathrm{fix}}$ (Jy)	$F_{\lambda,\mathrm{var}}$ (Jy)	R_{ap} (″)	$F_{\lambda,\mathrm{fix}}$ (Jy)	$F_{\lambda,\mathrm{var}}$ (Jy)	R_{ap} (″)	$F_{\lambda,\mathrm{fix}}$ (Jy)	$F_{\lambda,\mathrm{var}}$ (Jy)	R_{ap} (″)	$F_{\lambda,\mathrm{fix}}$ (Jy)	$F_{\lambda,\mathrm{var}}$ (Jy)	R_{ap} (″)	$F_{\lambda,\mathrm{fix}}$ (Jy)	$F_{\lambda,\mathrm{var}}$ (Jy)	R_{ap} (″)	$F_{\lambda,\mathrm{fix}}$ (Jy)	$F_{\lambda,\mathrm{var}}$ (Jy)	R_{ap} (″)
Herschel/PACS	160.0	180	180	11.2	677	677	32.0	⋯	⋯	⋯	2386	2386	32.0	622	622	14.4	655	655	12.8	10877	10877	48.0	1019	1019	25.6
		(264)	(264)		(825)	(825)					(2807)	(2807)		(886)	(886)		(783)	(783)		(12006)	(12006)		(1296)	(1296)	
Herschel/SPIRE	250.0	41	41	11.2	243	243	32.0	⋯	⋯	⋯	⋯	⋯	⋯	245	245	14.4	143	143	12.8	⋯	⋯	⋯	344	344	25.6
		(104)	(104)		(342)	(342)								(388)	(388)		(210)	(210)					(525)	(525)	
Herschel/SPIRE	350.0	10.17	10.17	11.2	75	75	32.0	⋯	⋯	⋯	429	429	32.0	61	61	14.4	25.39	25.39	12.8	1054	1054	48.0	91	91	25.6
		(31.72)	(31.72)		(120)	(120)					(594)	(594)		(113)	(113)		(51.61)	(51.61)		(1292)	(1292)		(177)	(177)	
Herschel/SPIRE	500.0	1.16	1.16	11.2	20.02	20.02	32.0	⋯	⋯	⋯	127	127	32.0	8.67	8.67	14.4	2.93	2.93	12.8	318	318	48.0	13.62	13.62	25.6
		(8.16)	(8.16)		(36.77)	(36.77)					(196)	(196)		(27.61)	(27.61)		(11.07)	(11.07)		(411)	(411)		(52.04)	(52.04)	

Notes. The value of flux density in the upper row is derived with background subtraction. The value in the bracket in the lower line is flux density derived without background subtraction.

[a] Flux density derived with a fixed aperture size of the 70 μm data.

[b] Flux density derived with wavelength-dependent variable aperture sizes.

[c] Aperture radius.

(This table is available in machine-readable form.)

also given the fact that this emission is at UV/optical/NIR wavelengths and is reprocessed by dust in the inner regions, including in the outflow, to longer wavelengths. The other half of the accretion energy is partly radiated from the disk and partly converted to the kinetic energy of the disk wind.

The density distribution of the disk wind is described by a semi-analytic solution, which is approximately a Blandford & Payne (1982) wind (see Appendix B of ZTM13), and the mass loading rate of the wind relative to the stellar accretion rate is assumed to be $f_w = \dot{m}_w/\dot{m}_* = 0.1$, which is a typical value for disk winds (Königl & Pudritz 2000). Such a disk wind carves out cavities from the core, which gradually open up as the protostar evolves. The opening angle of the outflow cavity is estimated following the method of Matzner & McKee (2000) by comparing the wind momentum and that needed to accelerate the core material to its escape speed (ZTH14). The accretion rate to the protostar is regulated by this outflow feedback.

The evolution of the protostar is solved using the model by Hosokawa & Omukai (2009) and Hosokawa et al. (2010) from the calculated accretion history. A shock boundary condition is used at very early stages when the accretion is quasi-spherical. However, then, for most of the evolution, a photospheric boundary condition is used, appropriate for disk accretion.

In the above modeling, the evolution of the protostar and its surrounding structures are all calculated self-consistently from the two initial conditions of the core: M_c and $\Sigma_{\rm cl}$. A third parameter, the protostellar mass, m_*, is used to specify a particular stage on these evolutionary tracks. In our current model grid (J. Zhang & Y. C. Tan 2017, in preparation), M_c is sampled at 10, 20, 30, 40, 50, 60, 80, 100, 120, 160, 200, 240, 320, 400, and 480 $M_\odot$, and $\Sigma_{\rm cl}$ is sampled at 0.10, 0.32, 1, and 3.2 g cm^{-2}, for a total of 60 evolutionary tracks. Then along each track, m_* is sampled at 0.5, 1, 2, 4, 8, 12, 16, 24, 32, 48, 64, 96, 128, and 160 $M_\odot$ (but on each track, the sampling is limited by the final achieved stellar mass, with star formation efficiencies from the core typically being ~0.5). There are then, in total, 432 physical models defined by different sets of (M_c, $\Sigma_{\rm cl}$, m_*).

Monte Carlo continuum radiation transfer simulations were performed for these models using the latest version of the HOCHUNK3d code by Whitney et al. (2003, 2013). The code was updated to include gas opacities, adiabatic cooling/heating, and advection (ZTM13). Various dust opacities are used for different regions around the protostar (see ZT11), following the choices of Whitney et al. (2003). For each model, 20 inclinations are sampled evenly in cosine space to produce the SEDs. To compare with the observations, a variable foreground extinction A_V is applied to the model SEDs. Also, the model SEDs are convolved with the transmission profiles of the various instrument filters to estimate flux densities in given observational bands.

We then use χ^2 minimization to find the best models to fit a given set of observations. The reduced χ^2 is defined as

$$\chi^2 = \frac{1}{N}\left\{\sum_{F_{\nu,\rm mod}>F_{\nu,\rm obs}}\left[\frac{\log_{10}F_{\nu,\rm mod}-\log_{10}F_{\nu,\rm obs}}{\sigma_u(\log_{10}F_{\nu,\rm obs})}\right]^2 + \sum_{F_{\nu,\rm mod}<F_{\nu,\rm obs}}\left[\frac{\log_{10}F_{\nu,\rm mod}-\log_{10}F_{\nu,\rm obs}}{\sigma_l(\log_{10}F_{\nu,\rm obs})}\right]^2\right\}. \quad (1)$$

When $F_{\nu,\rm obs}$ is an upper limit, we set $\sigma_l = \infty$, i.e., there is no contribution to χ^2 if $F_{\nu,\rm mod} < F_{\nu,\rm fit}$.

For each set of (M_c, $\Sigma_{\rm cl}$, m_*), we search for a minimum value of χ^2 by varying the inclination $\theta_{\rm view}$ and the foreground extinction A_V. The foreground extinction A_V is constrained within a range corresponding to 0.1 $\Sigma_{\rm cl}$ to 10 $\Sigma_{\rm cl}$, i.e., we assume that the foreground extinction is somewhat related to that expected from the ambient clump surrounding the core. We then compare the minimum χ^2 of different cases (M_c, $\Sigma_{\rm cl}$, m_*) to find the best models. Note that for our analysis in this paper we set the distance to be a known value, based on literature estimates. Therefore, our SED model grid has only five free parameters: M_c, $\Sigma_{\rm cl}$, m_*, $\theta_{\rm view}$, and A_V. Our intention is to then explore to what extent the observed SEDs can be explained by the different evolutionary stages of a relatively limited set of initial conditions of massive star formation from the Turbulent Core Model. We will show the results of the best five models for each source.

3.2.2. Robitaille et al. Models

We also fit the SEDs with the models of Robitaille et al. (2007) for comparison with the results of the ZT models. To do this, we use the SED fitting Python package *sedfitter*[13] developed by Robitaille et al. (2007). Note that in their fitting code they adjust the value of the data point to the middle of the error bar. This influence can be significant when the error bar is large and asymmetric.

We note that the Robitaille et al. models were developed mostly with the intention of fitting lower-mass protostars that are typically observed in lower pressure environments and with lower accretion rates than the massive protostars of the ZT models. There are ~30 output parameters in the Robitaille et al. models. The key parameters include stellar mass, stellar radius, stellar temperature, envelope accretion rate, envelope outer radius, envelope inner radius, envelope cavity-opening angle, viewing angle, bolometric luminosity, disk mass, disk outer radius, disk inner radius, disk accretion rate, extinction inside the model down to the stellar surface, centrifugal radius, envelope cavity density, and ambient density around the envelope, among others. We will show the results for some of these parameters—those directly comparable with the ZT models—for the best five Robitaille et al. models.

3.2.3. General SED Fitting Considerations

We fit the fiducial SEDs (with fixed aperture size and with background subtracted) with the ZT models and the Robitaille et al. (2007) models. The error bars are set to be the larger of either 10% of the background-subtracted flux density or the value of the estimated background flux density, for background-subtracted fluxes, given that order unity fluctuations in the surrounding background flux are often seen. However, we note that for the protostars analyzed here, which are relatively bright, background fluxes, especially at shorter wavelengths and through the peak of the SED, are small relative to the source. Thus, errors associated with background subtraction are typically not very significant for our analysis. The fitting procedure involves convolving model SEDs with the filter response functions for the various telescope bands. Source

[13] http://sedfitter.readthedocs.io/en/stable/

distances were adopted from the literature. For each source, we present the five best-fitting models.

Note that short wavelength fluxes, i.e., at $\lesssim$8 μm, may be affected by PAH emission and thermal emission from very small grains that are transiently heated by single photons. Neither of these effects are included in the ZT radiative transfer models. Therefore, we treat the data at these wavelengths as upper limit constraints on the models.

We also note that the SED model fitting performed here assumes that there is a single dominant source of luminosity, i.e., effects of multiple sources, including unresolved binaries, are not accounted for. This is a general limitation and caveat associated with this method. Depending on the scales at which apertures are defined and at which multiple sources may be present, secondary sources may already be identifiable in the analyzed MIR to FIR images. The SOFIA-FORCAST data used in this paper have angular resolutions of a few arcseconds, while the *Spitzer* IRAC 8 μm images have $\sim$2″ resolution. Occasionally, we have access to higher resolution ground-based MIR imaging of the sources. Future follow-up observations, e.g., with ALMA and VLA, can also help to assess the presence of multiple sources.

Finally, both sets of models used in this paper assume smoothly varying or constant accretion rates. The data being analyzed here were typically collected within a time frame of about 10 years (i.e., the *Spitzer*, *Herschel*, and SOFIA observations). There is evidence that protostars (e.g., Contreras Peña et al. 2017), including massive protostars (Caratti O Garatti et al. 2016; Hunter et al. 2017), can exhibit large luminosity fluctuations, probably due to bursts of enhanced accretion. However, especially for massive protostars, the event rate or duty cycle of such burst phases is not well constrained. Other aspects being equal, one expects that the luminosity fluctuations of massive protostars will be smaller than for low-mass protostars, since accretion luminosity makes a smaller fractional contribution to the total luminosity as protostellar mass increases (e.g., MT03, ZTH14).

4. Results

The SOFIA images for each source are shown in Section 4.1. Also, the type of multiwavelength data available for each source, the flux densities derived, and the aperture sizes adopted are listed in Table 2. $F_{\lambda,\mathrm{fix}}$ is the flux density derived with a fixed aperture size and $F_{\lambda,\mathrm{var}}$ is the flux density derived with a variable aperture size. The value of flux density listed in the upper row of each source is derived with background subtraction, while that derived without background subtraction is listed in brackets in the lower row.

4.1. Description of Individual Sources

Here we describe details about each source as well as presenting their SOFIA and ancillary imaging data.

4.1.1. AFGL 4029

The giant H II radio region W5 is divided into two subregions, W5-E and W5-W. W5-E is coincident with the molecular cloud IC 1848A, and on its eastern border lies the bright infrared region AFGL 4029. Beichman (1979) showed that AFGL 4029 is actually composed of two mid-IR sources, IRS1 and IRS2, which are separated by 22″. IRS2 appears to be a more evolved H II region containing a small stellar cluster dominated by a B1V star (Deharveng et al. 1997; Zapata et al. 2001). IRS1 is a luminous ($\sim10^4$ $L_\odot$) and highly reddened ($A_V\sim30$) MYSO (Deharveng et al. 1997), and has a radio component that has been given the designation G138.295 +1.555 (Kurtz et al. 1994). Later observations by Zapata et al. (2001) show IRS1 itself to be a binary radio source with a separation of 0.″5 (or 1000 au given the distance to the region of about 2.0 kpc (see, e.g., Deharveng et al. 2012). Deharveng et al. (1997) detect H_2 emission in the NIR emanating from IRS1 at a position angle of $\sim$265°, which is coincident with the high-velocity optical jet seen in [S II] (Ray et al. 1990). There also appears to be a smaller ($\sim$1″) radio jet at a similar angle ($\sim$270°) to the optical jet (Zapata et al. 2001), as well as a larger, high energy CO outflow (Ginsburg et al. 2011).

Though IRS1 is the source of interest to this work, both IRS1 and IRS2 are prominently detected in all four wavelengths of SOFIA (Figure 1). The diffuse and extended nature of IRS2 can be best seen in the 7 μm SOFIA data, consistent with flocculent morphology seen in the radio continuum maps (Zapata et al. 2001) and H and K' images (Deharveng et al. 1997). IRS1 appears to have a bright peak with a "tongue" of emission extending to the northwest at all SOFIA wavelengths. IRS1 has been observed at sub-arcsecond resolution in the MIR by Zavagno et al. (1999, 8–11 μm; de Wit et al. 2009, 24.5 μm), and it appears that this "tongue" is an arc-shaped concentration of dust emission, possibly related to the outflow cavity.

4.1.2. AFGL 437 (a.k.a. GL 437, G139.909+0.197, IRAS 03035+5819)

AFGL 437 is a compact infrared cluster (Wynn-Williams et al. 1981; Weintraub & Kastner 1996) that is dominated by four bright sources named AFGL 437 N, S, E, and W. Based on a combination of kinematic and spectroscopic distance measurements, Arquilla & Goldsmith (1984) estimated the distance to this region to be 2.0 kpc, and the total luminosity of the cluster is estimated to be $\sim3\times10^4$ $L_\odot$. Radio centimeter continuum emission was first detected from two of the sources, with most of the emission coming from source W (determined to be an H II region), with some weak emission coming from source S (Torrelles et al. 1992). In the infrared, Weintraub & Kastner (1996) found that source N could be resolved into two components, with the southeastern source of the two, dubbed WK 34, found to be the most embedded source in the cluster, and also associated with weak radio continuum emission.

This cluster of infrared sources is at the center of a CO molecular outflow (Gómez et al. 1992; Qin et al. 2008) that is roughly oriented north–south and poorly collimated, making it difficult to accurately determine which source(s) might be driving the outflow. Weintraub & Kastner (1996) found the cluster to be surrounded by an infrared reflection nebula that has a polarization pattern centro-symmetric with respect to source WK 34, which they believe traces an outflow cavity from that source. Kumar Dewangan & Anandarao (2010) resolve a finger-shaped "green fuzzy" emission region extending north from WK 34 in the *Spitzer* IRAC images, which they speculate is tracing H_2 emission from an outflow lobe (though such emission is not a dependable outflow tracer; see De Buizer & Vacca 2010 and Lee et al. 2013). Perhaps the most convincing evidence of an outflow from WK 34 comes from the *Hubble* NICMOS polarimetric imaging of this source (Meakin et al. 2005), which resolves a well-collimated bipolar reflection nebula that is oriented north–south and consistent

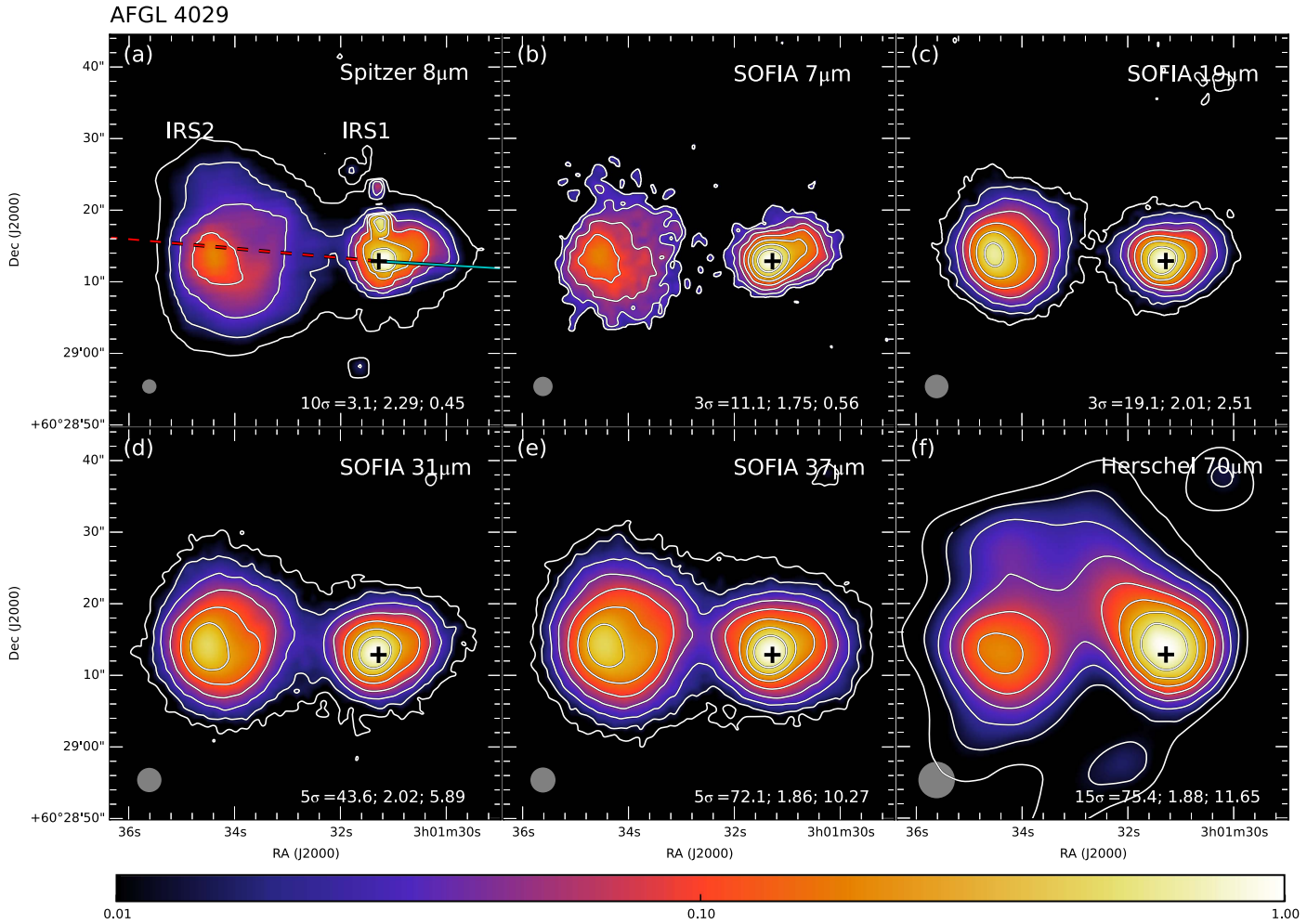

Figure 1. Multiwavelength images of AFGL 4029, with facility and wavelength given in the upper right of each panel. Contour level information is given in the lower right: the lowest contour level in number of σ above the background noise and corresponding value in mJy per square arcsec, then step size between each contour in $\log_{10}$ mJy per square arcsec, then peak flux in Jy. The color map indicates the relative flux intensity compared to that of the peak flux in each image panel, but only showing the signal above 3σ. Gray circles in the lower left show the resolution of each image. Sources IRS1 (target of interest of this paper) and IRS2 are labeled in panel (a). The black cross in all panels denotes the position of the radio source G138.295+1.555(S) from Zapata et al. (2001) at R.A.(J2000) = $03^{h}01^{m}31\overset{s}{.}28$, decl. (J2000) = $+60°29'12\overset{''}{.}87$. The lines in panel (a) show the outflow axis angle, with the solid span tracing the blueshifted direction and the dotted span tracing the redshifted direction. In this case, the outflow axis angle is from the H_2 and optical jet emission of Deharveng et al. (1997), and the blueshifted outflow direction is given by the CO observations of Ginsburg et al. (2011). In panel (a), the point sources to the north of the G138.295+1.555(S) position are ghosts in the *Spitzer* image and should not be interpreted as real structure. The data used to create this figure are available.

with the outflow observations described above. If this is the main source of outflow, previous SED modeling of WK 34 yields an estimated source mass and luminosity to be $\sim 7\,M_{\odot}$ and $\sim 1 \times 10^{3}\,L_{\odot}$, respectively (Kumar Dewangan & Anandarao 2010), which is more consistent with an intermediate-mass object than a true MYSO. We will see below that one of the favored ZT radiative transfer models includes a source with $m_{*} = 8\,M_{\odot}$, although higher-mass cases are allowed.

In the SOFIA data, we barely resolve source AFGL 437 N at 7 μm into WK 34 and its companion, but they are resolved in the *Spitzer* 8 μm data (Figure 2). We see no evidence of infrared emission to the north of WK 34 in the SOFIA data, which is where the green fuzzy emission has been seen. However, if the larger-scale CO outflow is being driven by WK 34, observations by Gómez et al. (1992) and Qin et al. (2008) show that the blueshifted outflow lobe should be to the south. The expectation would be that we should see the blueshifted outflow cavity more readily due to decreased extinction. Unfortunately, any southern outflow cavity from WK 34 cannot be discerned from the SOFIA data due to the resolution of the observations and the close proximity of source S to the south. However, the sub-arcsecond resolution 24.5 μm images from de Wit et al. (2009) conclusively show that there is no extended emission south of WK 34 at that wavelength (at least to within their detection limit).

Interestingly, the source with the peak infrared brightness is AFGL 437 S at the shorter MIR wavelengths, but at wavelengths longer than 19 μm, the UC H II region AFGL 437 W is where the brightness peaks (see also de Wit et al. 2009), perhaps further indicating that WK 34 is not an MYSO.

4.1.3. IRAS 07299–1651 (a.k.a. AFGL 5234, S302, DG 121, RCW 7, G232.62+01.00)

Figure 3 presents our standard multiwavelength data for IRAS 07299–1651. The NIR emission from this source was

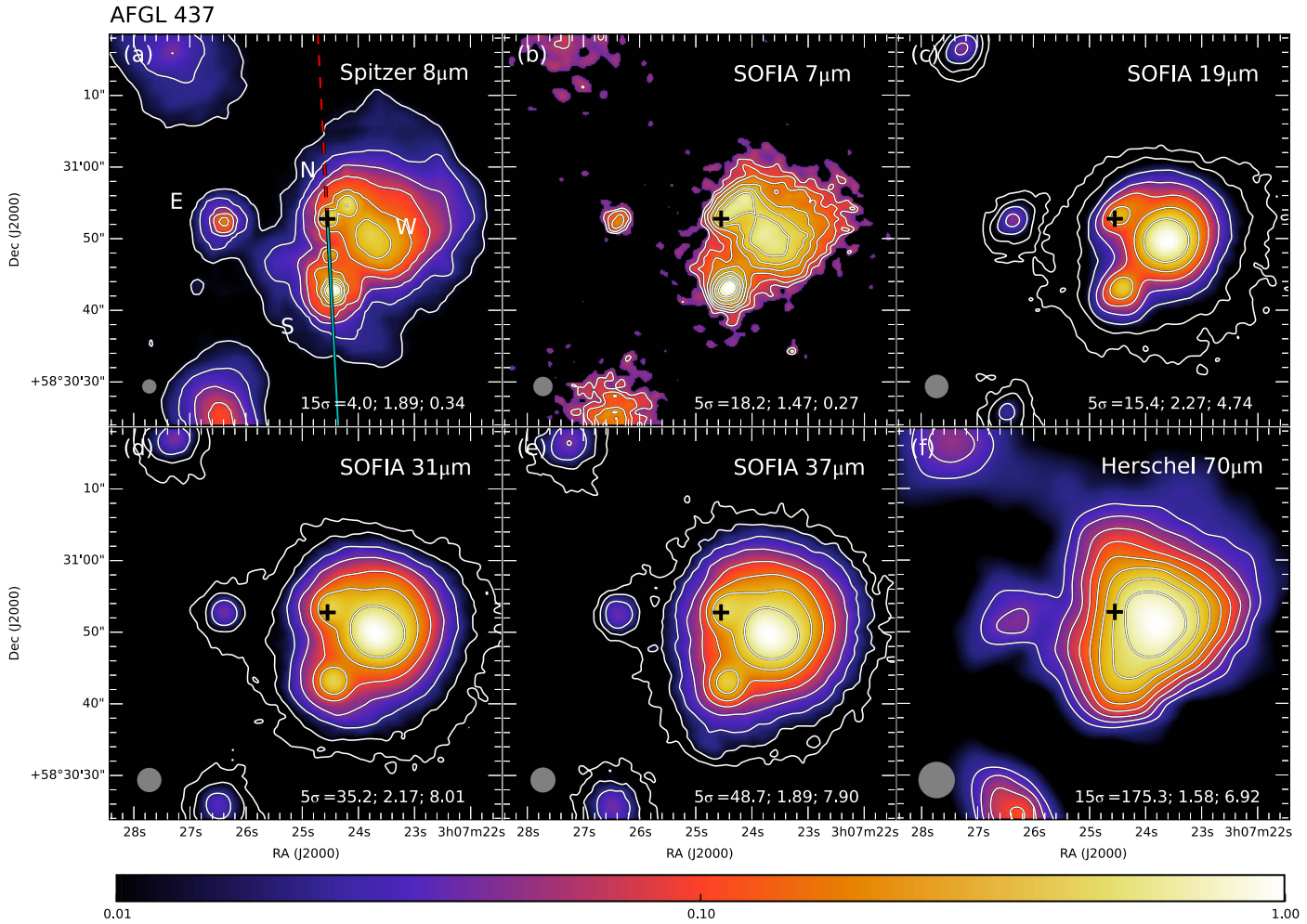

Figure 2. Multiwavelength images of AFGL 437, following the format of Figure 1. The location of the radio continuum source WK34 (Weintraub & Kastner 1996) is shown as a cross in all panels at R.A.(J2000) = $03^{h}07^{m}24\overset{s}{.}55$, decl.(J2000) = $+58°30'52\overset{''}{.}76$. The outflow axis angle is from the NIR bipolar emission angle from Meakin et al. (2005), and the blueshifted outflow direction is given by the CO observations of Gómez et al. (1992). The data used to create this figure are available.

shown to have a compact center with diffuse emission extended at a position angle of 305° (Walsh et al. 1999). Follow-up observations in the MIR in the *N*-band (∼10 μm) by Walsh et al. (2001) with the ESO Max Planck Institute 2.2 m telescope show a compact, perhaps slightly elongated source at this location. Our Gemini South 8 m observations at 11.7 μm at higher resolution and sensitivity show an elongated appearance resembling the NIR morphology, with a compact core and extended diffuse emission (see Figure 4). However, the MIR emission is not coincident with the NIR emission, and neither is coincident with the radio continuum peak of Walsh et al. (1998). The peak in emission in the *Spitzer* 8 μm image (Figure 3(a)) is coincident with the peak in the 11.7 μm Gemini image to within the accuracies of our astrometry ($\lesssim 0\overset{''}{.}5$).[14] As one looks to shorter wavelengths in the *Spitzer* IRAC data, the peak moves closer and closer to the 2 μm peak location, suggesting that extinction might be playing a role. At the resolution of SOFIA, the object looks rather point like, with a possible extension of the emission to the northwest seen at 31 and 37 μm (Figures 3(d) and (e)).

[14] This is different from the location of the peak seen in the *N*-band image of Walsh et al. (2001), which is likely in error.

Given the extended nature of the NIR and MIR emission of this target at high angular resolution, it was deemed a good candidate for being morphologically influenced by an outflow. The hypothesis is that the radio continuum source also drives an outflow, and the extended NIR and MIR emission are coming from the blueshifted outflow cavity. To date, however, there are no maps of outflow indicators of this source from which we may derive an outflow axis. Evidence of an outflow from this region does exist, including spectra that show that the ^{12}CO gas is considered to be in a "high-velocity" state (Shepherd & Churchwell 1996). Liu et al. (2010) mapped the integrated ^{13}CO emission at ∼1′ resolution and found it to be extended parallel and perpendicular to the NIR/MIR extension on the scale of ∼4′ in each direction. No velocity maps are presented in that work, and they claim that the emission is tracing a molecular core (not outflow), from which they estimate a gas mass of $1.2 \times 10^{3}\ M_{\odot}$.

De Buizer (2003) claimed that in some cases the groupings of 6.7 GHz methanol maser spots may lie in an elongated distribution that is parallel to the outflow axis for some MYSOs. Fujisawa et al. (2014) showed that the 6.7 GHz methanol maser spots are distributed over two groupings

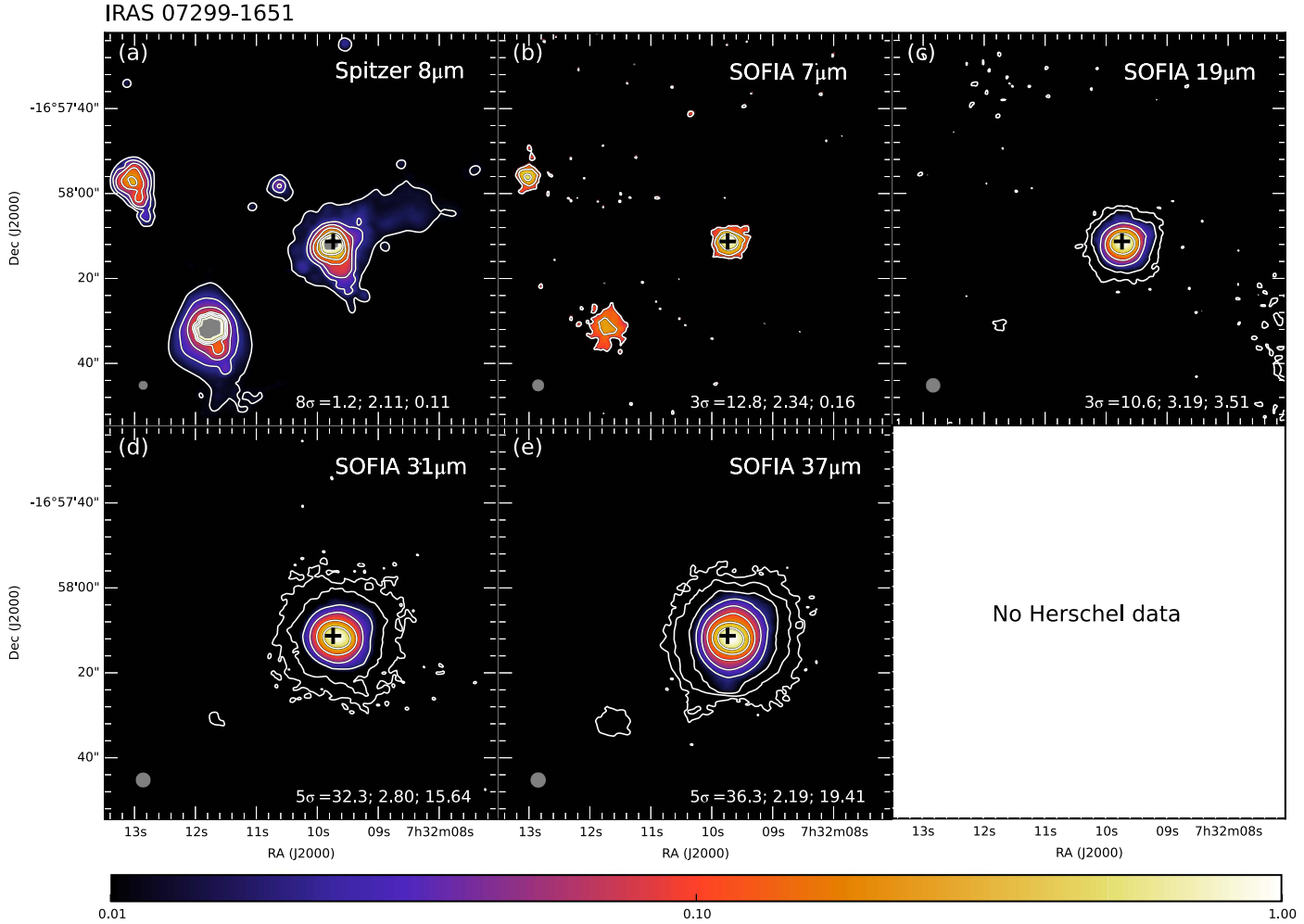

Figure 3. Multiwavelength images of IRAS 07299–1651, following the format of Figure 1. The gray areas in panel (a) are where the sources have saturated in the IRAC image. Also in panel (a) there are extensions to the southwest of the three brightest sources, which are ghosts that should not be interpreted as real structure. The location of the radio continuum source of Walsh et al. (1998) is shown as a cross in all panels at R.A.(J2000) = $07^{h}32^{m}09\overset{s}{.}74$, decl.(J2000) = $-16°58'11\overset{''}{.}28$. There are no outflow maps from which to discern an outflow angle or direction for this source. The data used to create this figure are available.

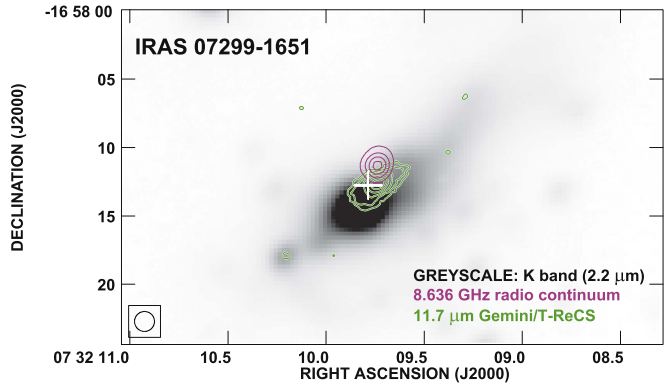

Figure 4. Image of IRAS 07299–1651 comparing the 11.7 μm Gemini/T-ReCS image (green contours) with the near-infrared (grayscale) and radio continuum (red contours) emission, as well as the methanol maser location (white cross) from Walsh et al. (1999).

separated by about 60 mas with a total distributed area of about 20 mas × 70 mas (or 40 au × 120 au, given the distance of 1.68 kpc estimated from the trigonometric parallax measurements of the 12 GHz methanol masers present in this source by Reid et al. 2009). Though there are two groups of masers, they have velocity gradients along their shared axis of elongation and are distributed at a position angle of 340°.

4.1.4. G35.20–0.74 (a.k.a. IRAS 18566+0136)

The G35.20–0.74 star-forming region, at a distance of 2.2 kpc (Zhang et al. 2009; Wu et al. 2014), was first identified as a star-forming molecular cloud through ammonia observations by Brown et al. (1982). Dent et al. (1985a) were the first to resolve the emission in this region into a molecular ridge running northwest to southeast seen in CS(2-1), with a nearly perpendicular outflow seen in CO(1-0). Dent et al. (1985b) found the NIR emission to be coming from an elongated north–south distribution. Heaton & Little (1988) observed this region in centimeter radio continuum and were able to resolve three compact sources arranged north–south, and concluded that the central source was likely a UC H II region while the north and south sources had spectral indices consistent with free–free emission from a collimated, ionized, bipolar jet. The orientation of this jet (P.A. ∼ 2°) appears to be different from that of the CO outflow (P.A. ∼ 58°), which has been interpreted either as evidence for precession of the ionized jet (Heaton & Little 1988; Little et al. 1998; Sánchez-Monge et al. 2014;

Beltrán et al. 2016), or multiple outflows from multiple sources (Gibb et al. 2003; Birks et al. 2006).

G35.20–0.74 was the first source observed among those in the SOMA survey sample, and the SOFIA-FORCAST imaging data were presented by Zhang et al. (2013a). These data helped define the infrared SED of the source, which implied an isotropic luminosity of $3.3 \times 10^4\ L_\odot$. However, modeling the emission (with early versions of the ZT radiative transfer models that had fixed outflow cavity-opening angles; ZTM13), including 10–40 μm intensity profiles, as being due to a single protostar driving an outflow along the N–S axis, Zhang et al. (2013a) derived a true bolometric luminosity in the range $\sim(0.7–2.2) \times 10^5\ L_\odot$, i.e., after correcting for foreground extinction and anisotropic beaming. Note, these estimates were based on a limited, ad hoc exploration of model parameter space. They correspond to protostellar masses in the range $m_* \simeq 20–34\ M_\odot$ accreting at rates $\dot{m}_* \sim 10^{-4}\ M_\odot\ \mathrm{yr}^{-1}$ from cores with initial mass $M_c = 240\ M_\odot$ in clump environments with $\Sigma_{\rm cl} = 0.4–1.0\ \mathrm{g\,cm^{-2}}$ and with foreground extinctions from $A_V = 0–15$ mag.

Such an interpretation of outflow orientation is broadly consistent with the sub-arcsecond VLA observations of this field by Gibb et al. (2003) at centimeter wavelengths, which show that the three concentrations of radio continuum emission from Heaton & Little (1988) break up into 11 individual knots all lying along a north–south position angle. The central source itself is resolved into two sources separated by 0.″8. The northern of the two central sources (source 7) has a spectral index typical of a UC H II region and was claimed by Gibb et al. to be the most likely driving source of the radio jet. Beltrán et al. (2016) have also identified this source, a component of a binary system they refer to as 8a, as the likely driving source. To be able to ionize the UC H II region, Beltrán et al. (2016) estimate that it have the H-ionizing luminosity of at least that of a spectral type B1 zero age main sequence (ZAMS) star. This radio source is coincident with Core B of Sánchez-Monge et al. (2014) seen at 870 μm with ALMA (which is the same as source MM1b from the 880 μm *SMA* observations of Qiu et al. 2013), who estimate the core mass in this vicinity to be $18\ M_\odot$.

The scenario of north–south directed protostellar outflows is also supported by MIR imaging. High-resolution MIR images of this region by De Buizer (2006) showed that the emission is peaked to the north of radio source 7 and elongated in a north–south orientation, very similar to what was seen in the NIR for the first time by Dent et al. (1985b). A weak extended area of emission was seen to the south, and can be seen in the much more sensitive *Spitzer* 8 μm data (Figure 5(a)). The outflow/jet is blueshifted to the north (e.g., Gibb et al. 2003; Wu et al. 2005) and is likely to be the reason why we see emission predominantly from that side of source 7 at shorter MIR wavelengths. However, as discussed by Zhang et al. (2013a), the longer wavelength SOFIA images (Figure 5) are able to detect emission also from the southern, far-facing outflow cavity.

Finally, we note that for G35.20–0.74, we could not derive an accurate background-subtracted flux density for the Gemini data with the fixed aperture size due to the small size of the images. Thus, in this case we estimate a background-subtracted flux density derived from a smaller aperture size.

4.1.5. G45.47+0.05

G45.47+0.05 was first detected as a UC H II region in the radio continuum at 6 cm (Wood & Churchwell 1989) and lies at a distance of 8.4 kpc, based upon the trigonometric parallax measurements of masers in nearby G45.45+0.05 (Wu et al. 2014). G45.47+0.05 has a relatively high luminosity ($\sim 10^6\ L_\odot$; Hernández-Hernández et al. 2014), testifying to its nature as an MYSO. The UC H II region is also coincident with other MYSO tracers like hydroxyl and water masers (Forster & Caswell 1989).

There is some debate as to the nature of the outflow and driving source in this region. *Spitzer* IRAC images show a source that is a bright "green fuzzy," and consequently was categorized as being a "likely MYSO outflow candidate" in the work of Cyganowski et al. (2008). However, Lee et al. (2013) find no H_2 emission component to the green fuzzy and classify the NIR emission as a reflection nebula (possibly from an outflow cavity). This region was mapped in HCO^+(1-0), a potential outflow indicator, by Wilner et al. (1996), who showed that the emission is oriented roughly north–south (P.A. $\sim 3°$) and centered on the location of the UC H II region, with blueshifted emission to the north. They also mapped the area in another outflow indicator, SiO(2-1), and find emission at the location of the UC H II region with a single blueshifted component lying $\sim 14''$ to the northwest at a position angle of about $-25°$ (see Figure 6). However, Ortega et al. (2012) mapped the area in ^{12}CO(3-2) and found the red and blueshifted peaks to be oriented at an angle of $\sim 15°$, but with an axis offset $\sim 10''$ southeast of the UC H II region.

The observations of De Buizer et al. (2005) first showed that the MIR emission in this region is offset $\sim 2.''5$ northwest of the radio continuum peak. *Spitzer* IRAC and 2MASS data confirm this offset of the peak of the NIR/MIR emission, and show a similar extended morphology, with the axis of elongation oriented at a position angle of about $-30°$ and pointing radially away from the radio continuum peak. The SOFIA data (Figure 6) show this same morphology at wavelengths greater than 19 μm (the 11 μm SOFIA observation is a shallow integration that only barely detects the peak emission from the source). We also present higher angular resolution Gemini T-ReCS imaging at 11.7 and 18.3 μm in Figure 7, which also shows this offset and elongation. We note that the elongated morphology persists out to even longer wavelengths, as seen in both the *Herschel* 70 μm data, as well as *JCMT* SCUBA images at 850 μm (Hernández-Hernández et al. 2014).

There are two main scenarios to describe the outflow and driving source in this region. The first is that the massive star(s) powering the UC H II region is (are) also driving a roughly north–south outflow, with the CO, HCO^+, and SiO emission tracing different parts of the wide-angled outflow. The NIR and MIR emission are emerging from the blueshifted outflow cavity. The slight offset between the UC H II region peak and the NIR/MIR emission may be due to the high extinction toward the UC H II region itself. High spatial resolution adaptive optics imaging in the NIR of this source (Paron et al. 2013) show it to be a triangular-shaped emission region, with its southern apex pointing directly back at the UC H II region location. The opening angle of this outflow cone is $\sim 50°$, with its axis of symmetry pointing toward the blueshifted SiO emission, hinting that this might be a cone-shaped outflow cavity/reflection nebula emanating from the UC H II region. Furthermore, while the SOFIA 11 μm

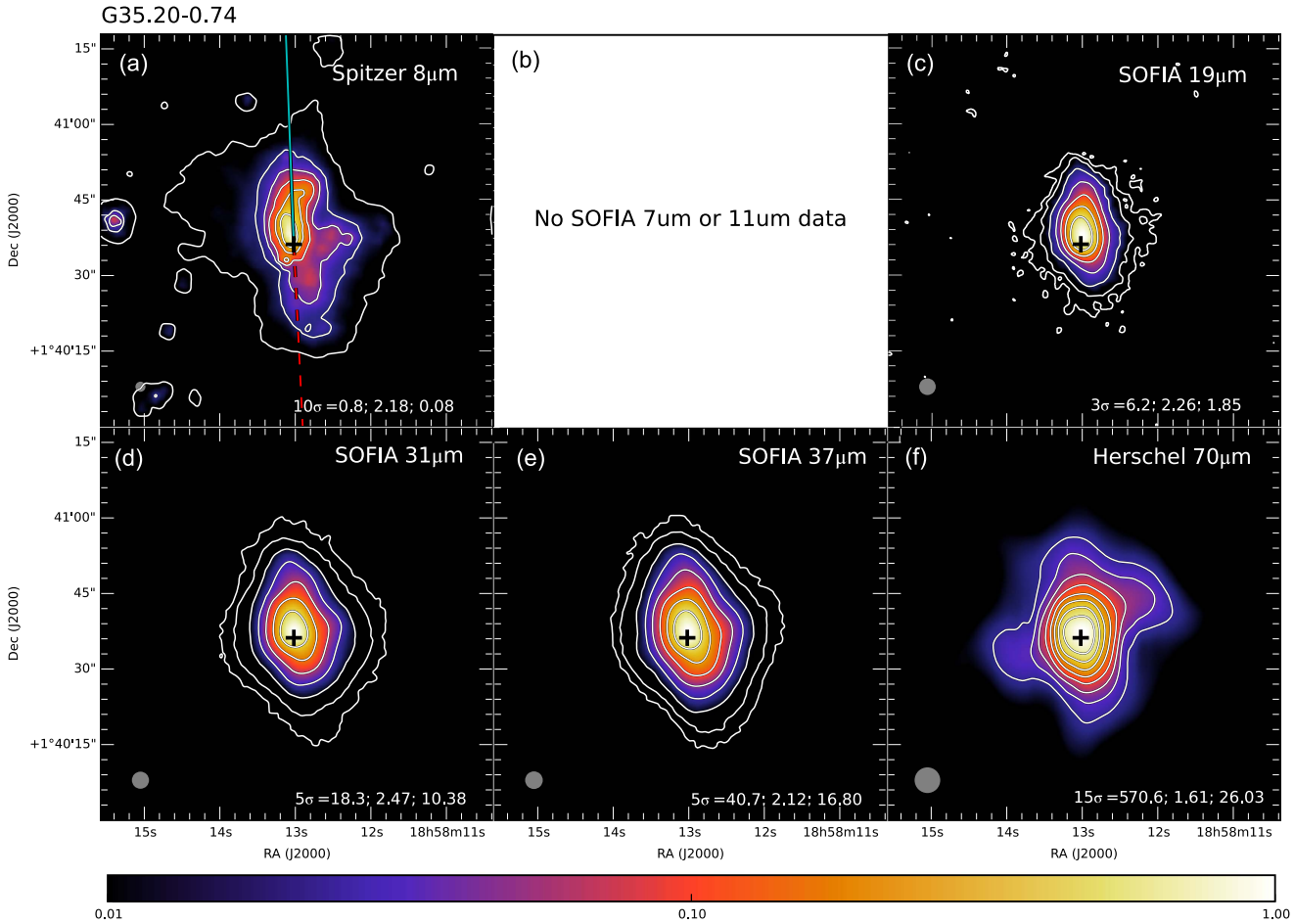

Figure 5. Multiwavelength images of G35.20–0.74, following the format of Figure 1. The location of radio continuum source 7 from Gibb et al. (2003) is shown as a cross in all panels at R.A.(J2000) = $18^{h}58^{m}13\overset{s}{.}02$, decl.(J2000) = $+01°40'36\overset{''}{.}2$. In panel (a) the axis of the radio jet is shown (Gibb et al. 2003); the blueshifted direction is derived from CO observations of Birks et al. (2006). The data used to create this figure are available.

emission is peaked close to the MIR and NIR peaks seen by *Spitzer* and 2MASS, the peak of the longer wavelength MIR emission is centered closer to the UC H II region peak, as would be expected in this scenario. It is not clear that we are detecting any additional emission from the redshifted outflow cavity, even at the longest SOFIA wavelengths.

The second scenario is that the outflow is coming from an NIR star at the western apex of the triangular-shaped NIR-emitting region seen in the adaptive optics images of Paron et al. (2013). They dub this source 2MASS J19142564 +1109283 (see Figure 6(a)), which is actually the name of the entire NIR-emitting region (2MASS did not have the resolution to separate this stellar source from the rest of the extended emission). In this scenario, the outflow cone from 2MASS J19142564+1109283 would have a much wider opening angle of about ∼90° and have an axis of symmetry that points toward the blueshifted ^{12}CO(3-2) peak seen by Ortega et al. (2012). This scenario is not favored here because it does not explain the location of the southern redshifted ^{12}CO outflow peak, which would be at an angle ∼80° from the outflow axis, nor does it explain the roughly north–south outflow emission seen in HCO^{+}(1-0) and SiO(2-1).

Whether the driving source is a stellar object at the center of the UC H II region or 2MASS J19142564+1109283, it appears that the MIR emission observed in the region is coming from a blueshifted outflow cavity.

4.1.6. IRAS 20126+4104 (a.k.a. G078.12+03.64)

At a distance of 1.64 kpc (Moscadelli et al. 2011) in the Cygnus-X star-forming region, IRAS 20116+4104, along with G35.20–0.74, could be considered a prototypical example of an MYSO with an outflow, and consequently, there have been numerous studies directed toward this object. Observations suggest a luminosity of $1.3 \times 10^{4}\ L_{\odot}$ with a central protostar having an estimated mass of 7 to 12 $M_{\odot}$ (Cesaroni et al. 1997; Keto & Zhang 2010; Johnston et al. 2011; Chen et al. 2016). This source is surrounded by a resolved accretion disk, believed to be undergoing Keplerian rotation (Cesaroni et al. 1997, 1999, 2005) at a position angle of ∼53°. Though IRAS 20116+4104 appears to be an MYSO, it might be too young to have produced a UC H II region; radio continuum emission observations at centimeter wavelengths show that the emission components near the center of the outflow are consistent with free–free emission from ionized gas in an outflow. The location of the driving source of the outflow was determined through proper motion studies of water masers, which seem to be moving away from a common location (Moscadelli et al. 2011). This location is coincident with the

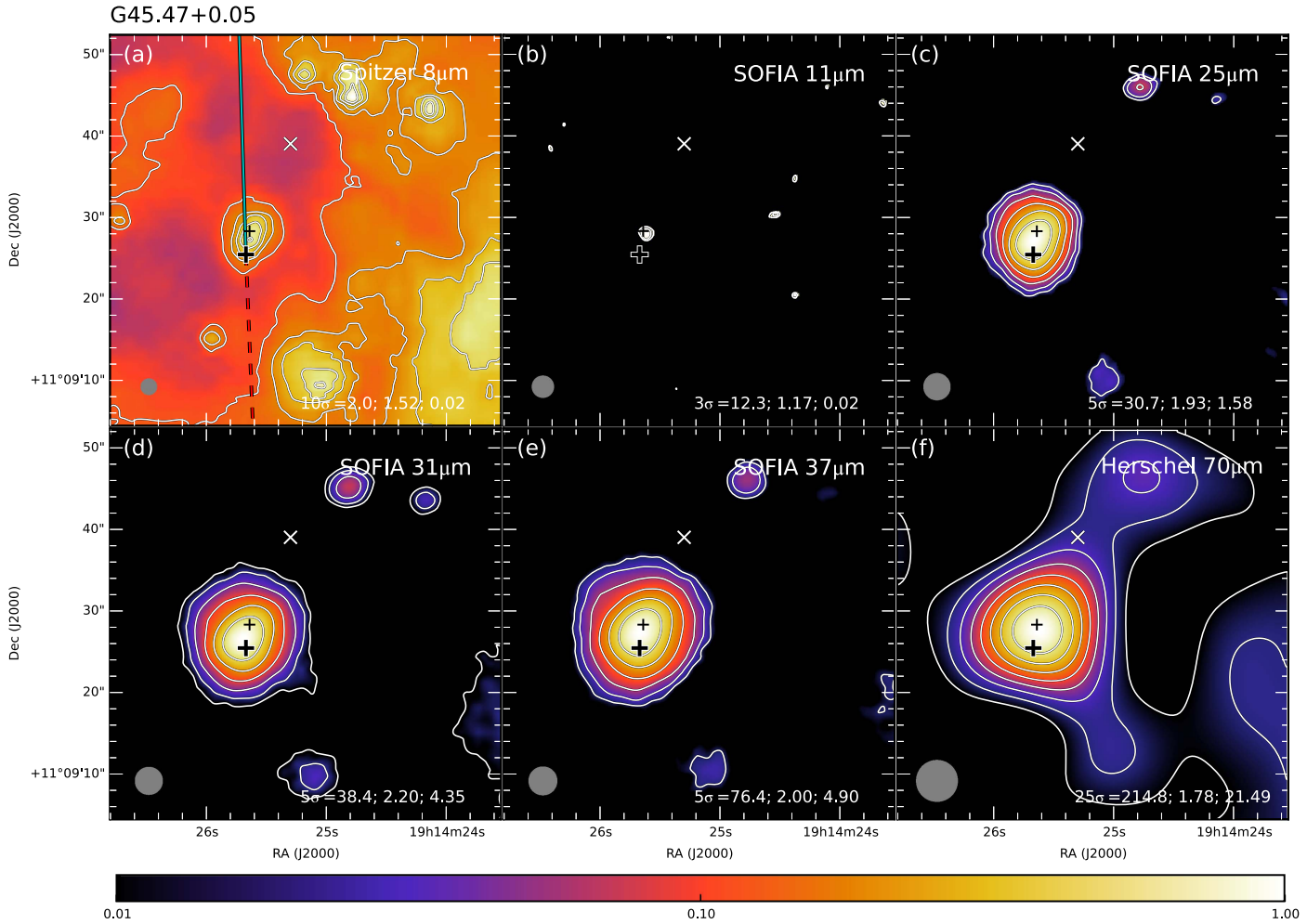

Figure 6. Multiwavelength images of G45.47+0.05, following the format of Figure 1. The location of the 6 cm radio continuum peak of the UC H II region of White et al. (2005) is shown as a large cross in all panels at R.A.(J2000) = $19^{h}14^{m}25\overset{s}{.}67$, decl.(J2000) = $+11°09'25\overset{''}{.}45$. The location of the 2MASS source J19142564 +1109283 is shown by the small cross. The location of the peak of the blueshifted SiO(2-1) emission of Wilner et al. (1996) is shown by an ×. The outflow axis angle and the blueshifted outflow direction are given by the HCO^{+} observations of Wilner et al. (1996). The data used to create this figure are available.

center of the accretion disk as delineated by CH_3CN(12-11) emission from Cesaroni et al. (1999).

IRAS 20126+4104 has a well-collimated bipolar molecular outflow oriented at an angle roughly perpendicular to the disk (P.A. ∼ 115°) with an inclination angle of the outflow axis to the plane of the sky of only ∼10° (Zhang et al. 1999; Hofner et al. 2007; Su et al. 2007; Moscadelli et al. 2011; see also Cesaroni et al. 2013). De Buizer (2007) made the first suggestion that the extended MIR emission observed toward this source might be related to the outflow.

At wavelengths greater than 19 μm, SOFIA data (Figure 8) show an elongated morphology at an angle (P.A. ∼ 125°) similar to that of the outflow (the 11 μm SOFIA observation is a shallow integration that only barely detects the peak emission from the source). Even the *Herschel* 70 μm data show an elongation along this outflow axis direction. The location of the driving source from Moscadelli et al. (2011) is coincident with the MIR/FIR peak (to within astrometric accuracy), and the amount of extended emission seen to the NW of this peak is comparable to that seen to the SE. This symmetry may be expected since the outflow is oriented almost in the plane of the sky, and consequently there should be little bias of emission from just the blueshifted lobe.

4.1.7. Cepheus A

Cep A contains a massive bipolar molecular outflow primarily aligned east–west that was initially identified by Rodriguez et al. (1980); however, at higher spatial resolutions, the outflow morphology is quite complex. The central ∼2′ of the outflow appears to be dominated by components aligned NE–SW (Bally & Lane 1990; Torrelles et al. 1993; Narayanan & Walker 1996; Gómez et al. 1999; Zapata et al. 2013). This central region contains a compact, extremely high-velocity CO outflow (Narayanan & Walker 1996) with an axis at a position angle of ∼50° that is believed to trace a younger component than the rest of the outflow (Cunningham et al. 2009). This central outflow component appears to have an axis close to the plane of the sky but with blueshifted emission to the NE (Gómez et al. 1999; Zapata et al. 2013). At NIR wavelengths, the region displays an extremely bright reflection nebula (Cunningham et al. 2009), almost wholly contained within this blueshifted outflow cavity.

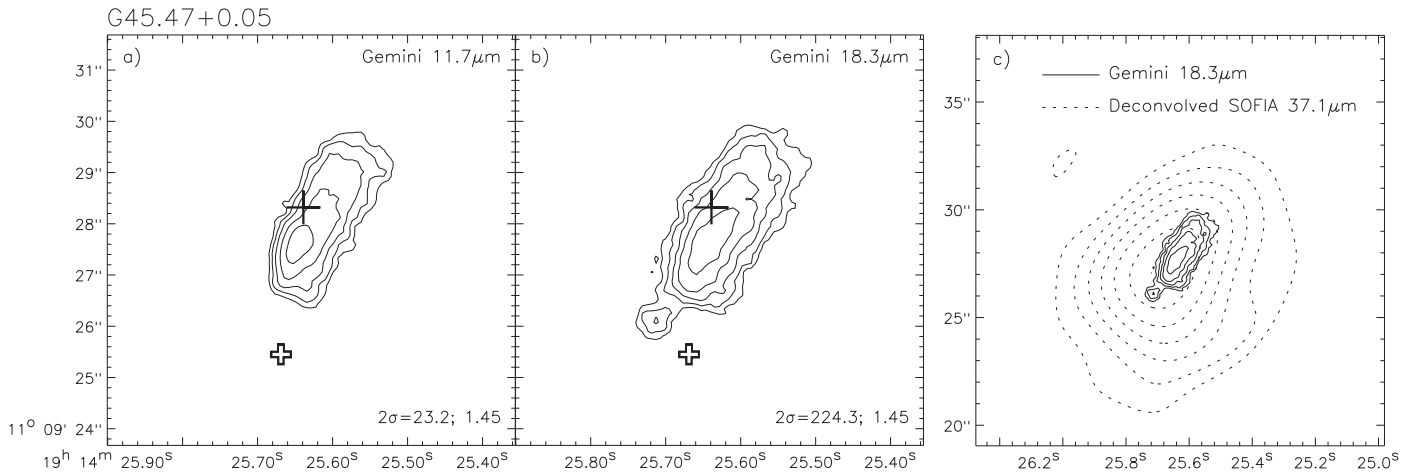

Figure 7. Sub-arcsecond resolution MIR images of G45.47+0.05 from Gemini T-ReCS. Symbols and annotation are the same as in Figure 6.

At the center of this outflow is a cluster of radio sources, and there is confusion as to which source(s) might be driving the outflow(s) (Zapata et al. 2013). One of the main candidates for driving the outflow, and the brightest radio continuum source in the region, is HW 2 (Hughes & Wouterloot 1984). It has a luminosity of about $10^4\ L_\odot$ (Garay et al. 1996), suggesting it is a B0.5 star approaching $20\ M_\odot$, given a distance to the source of 700 pc based on parallax measurements of 12 GHz methanol masers in the region (Moscadelli et al. 2009) and of radio source HW 9 (Dzib et al. 2011). HW 2 has not been detected at NIR wavelengths (Casement & McLean 1996; Cunningham et al. 2009; Jones et al. 2004), nor in the MIR (De Buizer et al. 2005; de Wit et al. 2009; also Cunningham et al. 2009; however, the absolute astrometry of their MIR images, and hence the placement of radio sources with respect to the MIR sources, appears to be off by over 6″).

The estimated extinction to the region around HW 2 is $A_V \sim 300$–1000 mag (Goetz et al. 1998; Cunningham et al. 2009), and therefore it is not surprising it is not directly detected in the NIR, MIR, or in our SOFIA data (Figure 9). However, it does appear that the contour peak shifts toward this location in the 70 μm *Herschel* data (Figure 9(f)).

At 7 μm the emission seen by SOFIA corresponds well to the NIR reflection nebula and blueshifted outflow cavity. As one goes to longer SOFIA wavelengths, we begin to see increasingly brighter emission to the SW, which corresponds to the direction of the redshifted outflow. We suggest that we are beginning to penetrate the higher extinction toward this region and the emission we are seeing at wavelengths >30 μm is coming from the redshifted outflow cavity.

4.1.8. NGC 7538 IRS 9

NGC 7538 is an optically visible H II region (Fich & Blitz 1984) located at a distance of 2.65 kpc, as determined from trigonometric parallax measurements (Moscadelli et al. 2009). Infrared observations of this region by Wynn-Williams et al. (1974) and Werner et al. (1979) led to the identification of multiple discrete sources in the vicinity of the optical nebula, which were named IRS 1 through 11. The source IRS 9 lies ∼2′ to the SE of the prominent and well-studied IRS 1 region. It powers its own reflection nebula, and has a total luminosity of about $3.5 \times 10^4\ L_\odot$ (Sandell et al. 2005; corrected to the distance from Moscadelli et al. 2009), which is the equivalent of a B0.5 ZAMS star.

Though IRS 9 has the luminosity of a typical MYSO, it has very weak radio continuum emission. Sandell et al. (2005) found that the object has a flat radio spectrum consistent with free–free emission from a collimated, ionized jet. They also disentangled the rather complex structures seen in various outflow tracers into distinct outflows from three different sources, suggesting a cluster associated with IRS 9. The outflow associated most closely with the position of IRS 9 itself was measured to have a very high velocity (Mitchell & Hasegawa 1991), leading to the suggestion that we might be observing the system nearly face-on (Barentine & Lacy 2012). The high spatial resolution (∼6″) HCO^+ maps of Sandell et al. (2005) show that IRS 9 indeed drives a bipolar, extremely high-velocity outflow approximately oriented E–W (P. A. ∼ 85°) that is inclined by only ∼20° to the line of sight. Given this orientation, the outflow lobes seen in HCO^+ do not extend very far from IRS 9 in projection (∼14″), but the blueshifted outflow lobe is clearly to the west of IRS 9, and the redshifted outflow lobe to the east (Figure 10(a)). We note here that the best-fitting ZT and Robitaille et al. radiative transfer models for this system (presented below), based solely on SED fitting, have viewing angles of about 20° to the outflow axis, very similar to the above estimates based on outflow observations.

Our SOFIA data for this source look rather point like at 7 μm; however, beginning at 19 μm, the source begins to show signs of being elongated in an E–W orientation, similar to the outflow axis (Figure 10). The *Herschel* 70 μm data also show a more prominent east–west elongation with a larger extension to the west in the direction of the blueshifted outflow cavity.

4.2. General Results from the SOFIA Imaging

In addition to the monochromatic images presented above, we also construct three-color images of all the sources, presented together in Figure 11. The three-color images reveal color gradients across the sources: i.e., the more extincted, far-facing outflow cavities appear redder, with this morphology particular clear in the cases of G35.20–0.74 and Cep A. Note, however, that these RGB images have different beam sizes for

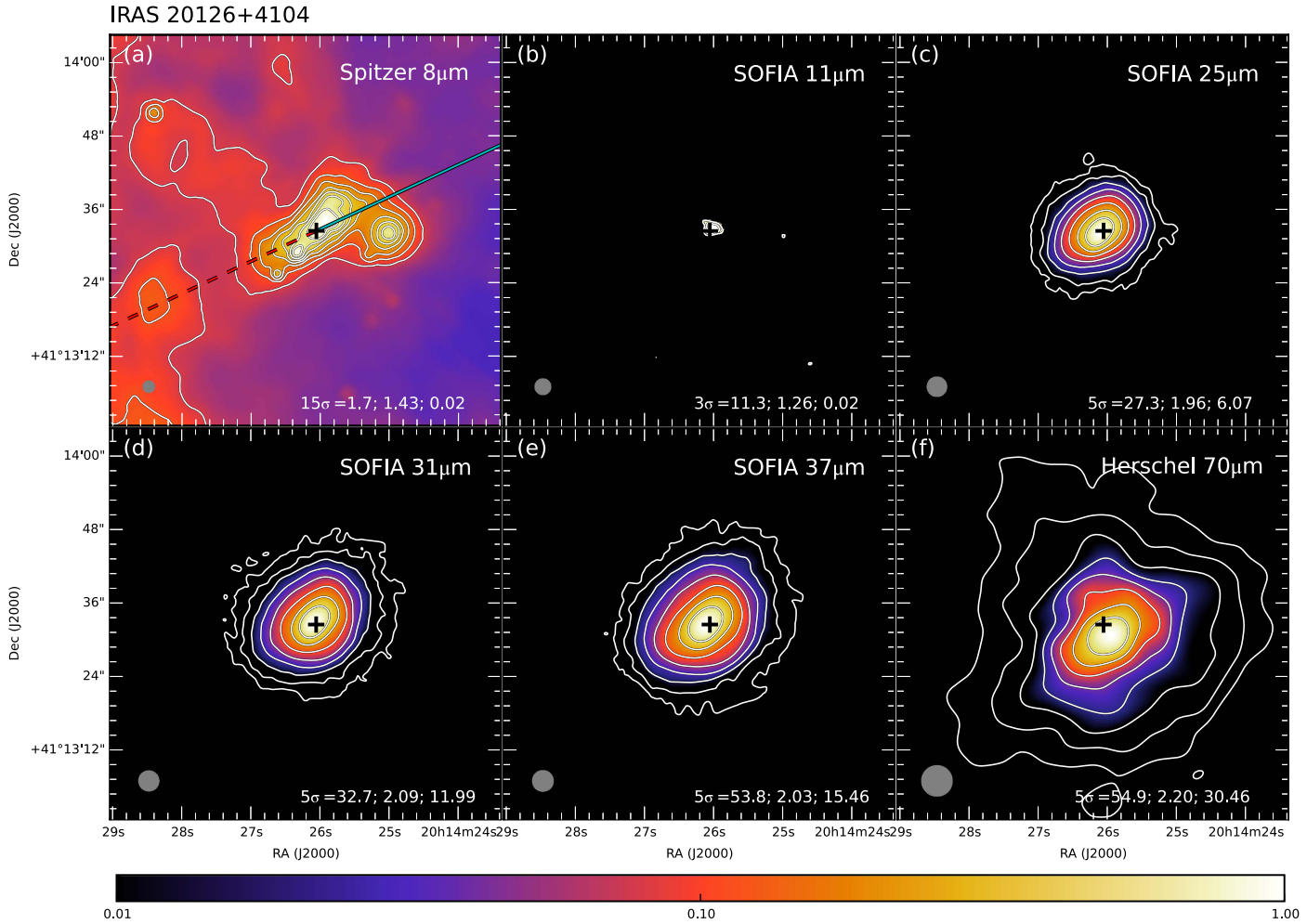

Figure 8. Multiwavelength images of IRAS 20126+4104, following the format of Figure 1. The nominal location of the protostar, derived from the model fit to the proper motions of the water masers from Moscadelli et al. (2011), is shown as a large cross in all panels at R.A.(J2000) = $20^{h}14^{m}26\overset{s}{.}05$, decl.(J2000) = $+41°13'32\overset{''}{.}48$. The outflow axis angle and the blueshifted outflow direction are given by the HCO^{+} observations of Cesaroni et al. (1999). The data used to create this figure are available.

the different colors (especially blue), with the effect being to tend to give small sources an extended red halo.

G35.20–0.74 was the first source observed for this survey, and it has been the subject of its own paper (Zhang et al. 2013a) describing how the outflow from this massive protostar is likely to directly influence the morphology we see at infrared wavelengths. The hypothesis is that massive stars form in dense cores, with extinctions of $A_V \gtrsim$ hundreds of magnitudes along the line of sight to the central protostar. Outflows are driven by accretion and can effectively clear out material surrounding the core along the outflow axis direction, significantly decreasing extinction in those directions. Thus, radiation readily leaves via these cavities, and if the orientation to our line of sight is favorable, we can detect more intense and shorter wavelength infrared emission from these sources. Blueshifted outflow cavities appear brighter. However, as one observes at longer wavelengths, it becomes possible to see emission from the redshifted outflow cavities. The previous subsection discussed the observational evidence that indicates that each of the regions in our sample contains a high- or intermediate-mass protostar driving an outflow. How widespread is the evidence in our sample that the MIR morphologies are influenced by the presence of these outflow cavities?

Of the eight sources in our sample, only AFGL 437 does not show clear signs of extended MIR/FIR emission. Of the remaining seven sources, we can conclude that six are extended in their MIR/FIR emission at a position angle comparable to the orientation of their outflow axes. The only exception is IRAS 07299–1651, and this is only excluded because no outflow maps exist for this source. However, since it displays a behavior in morphology as a function of wavelength similar to the rest of the sources, we predict that an outflow is present at a position angle of ~300°, with a blueshifted lobe to the SE. For two of the sources in the sample, it appears that their MIR/FIR emission is extended only to one side of the central stellar source: AFGL 4029 and G45.47+0.05. In both cases, this emission is on the blueshifted side. Three sources appear to be extended to one side at shorter wavelengths and more symmetrically extended at longer wavelengths: G35.20–0.74, IRAS 20126+4104, and Cepheus A. In all three cases, the emission at shorter wavelengths comes predominantly from the blueshifted side of the outflow. The remaining source is NGC 7538 IRS 9, for which, perhaps because of an almost pole-on outflow orientation, we only see modest amounts of

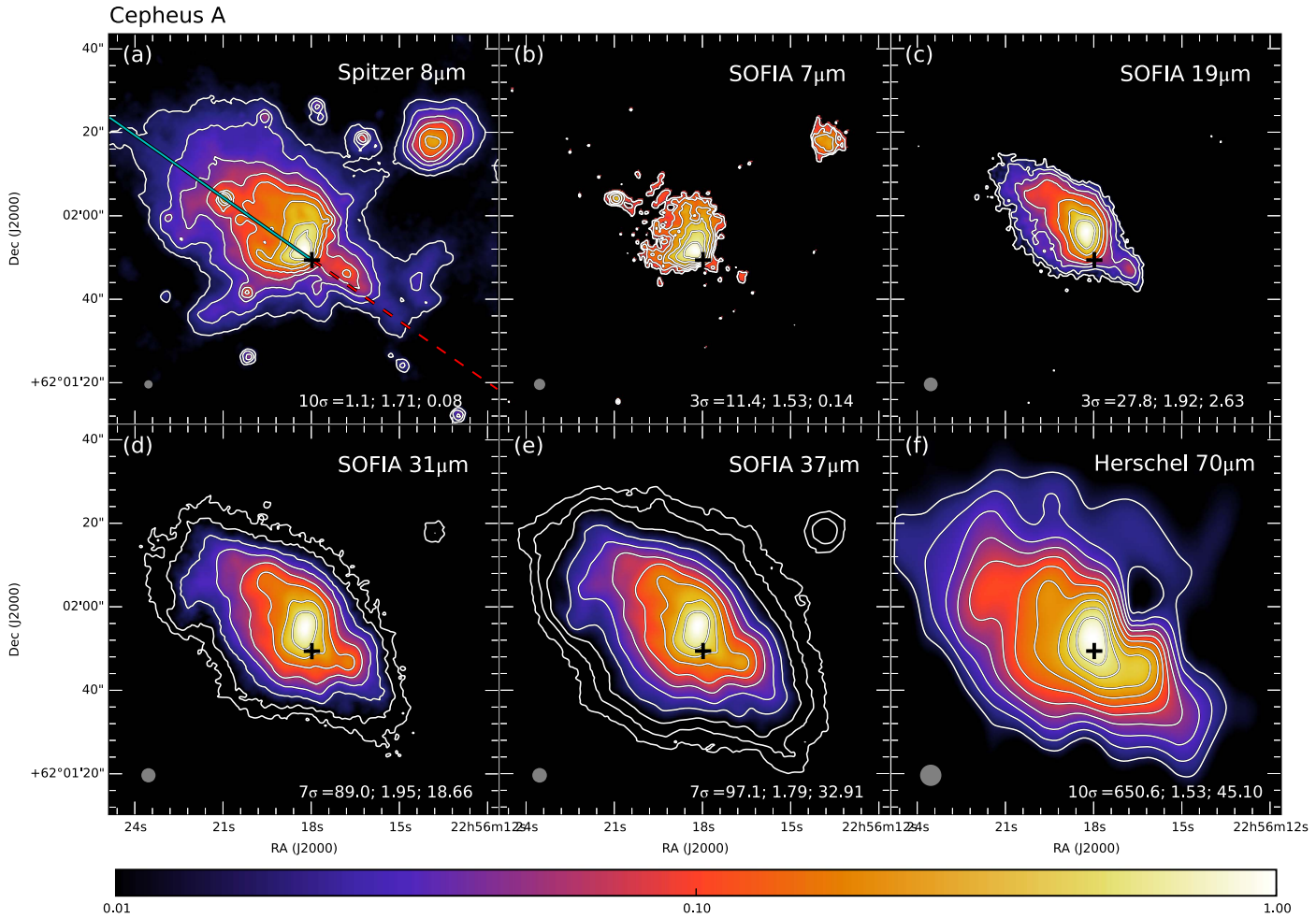

Figure 9. Multiwavelength images of Cepheus A, following the format of Figure 1. The cross in each panel shows the location of the radio continuum source HW 2 at R.A.(J2000) = $22^{h}56^{m}17\overset{s}{.}98$, decl.(J2000) = $+62°01'49\overset{''}{.}39$. The outflow axis angle and the blueshifted outflow direction are given by the HCO^{+} observations of Gómez et al. (1999). The data used to create this figure are available.

extended MIR/FIR emission. However, the little MIR/FIR extension that is seen is at the angle of the projected outflow axis. Somewhat surprising, however, is that the elongated morphologies seen at 7–40 μm are also present in most cases in the *Herschel* 70 μm images, showing that outflows can impact protostellar appearance even at such long FIR wavelengths.

Thus, the first eight sources of the SOMA Star Formation survey give strong support to the hypothesis that MIR to FIR morphologies of high- and intermediate-mass protostars are shaped by their outflow cavities. Bipolar, oppositely directed outflows are a generic prediction of Core Accretion models. The presence of dense core envelope gas near the protostar will tend to extinct shorter wavelength light to a greater degree so that the emission peaks at these wavelengths appear displaced away from the protostar toward the blueshifted, near-facing side of the outflow. This qualitative prediction again appears to be confirmed by our survey results. MIR to FIR morphologies thus give important information about how massive protostars are forming, especially the orientation and structure of their outflow cavities and the presence of dense core envelopes. In the following section, we use SOFIA and other data to make more quantitative assessments of the properties of these protostars.

4.3. Results of SED Model Fitting

Here we focus on simple SED model fits to the sample, deferring the fitting of image flux profiles to a future paper. We will compare the results derived from the ZT model grid with those from the Robitaille et al. grid.

4.3.1. The SEDs

Figure 12 shows the SEDs of the eight sources that have been discussed in this paper. The figure illustrates the effects of using fixed or variable apertures, as well as the effect of background subtraction. Our fiducial method is that with fixed aperture and with background subtraction carried out. This tends to have moderately larger fluxes at shorter wavelengths than the variable aperture SED. However, the $\lesssim$8 μm flux is in any case treated as an upper limit in the SED model fitting, given the difficulties of modeling emission from PAHs and transiently heated small grains. Apart from IRAS 07299–1651, which lacks *Herschel* data, all of the SEDs are well characterized: in particular, the peaks are well covered by the combination of SOFIA-FORCAST and *Herschel* PACS and SPIRE data.

We note that in the case of G35.20–0.74, our derived fiducial SED differs modestly ($\lesssim$20%) from that estimated by Zhang

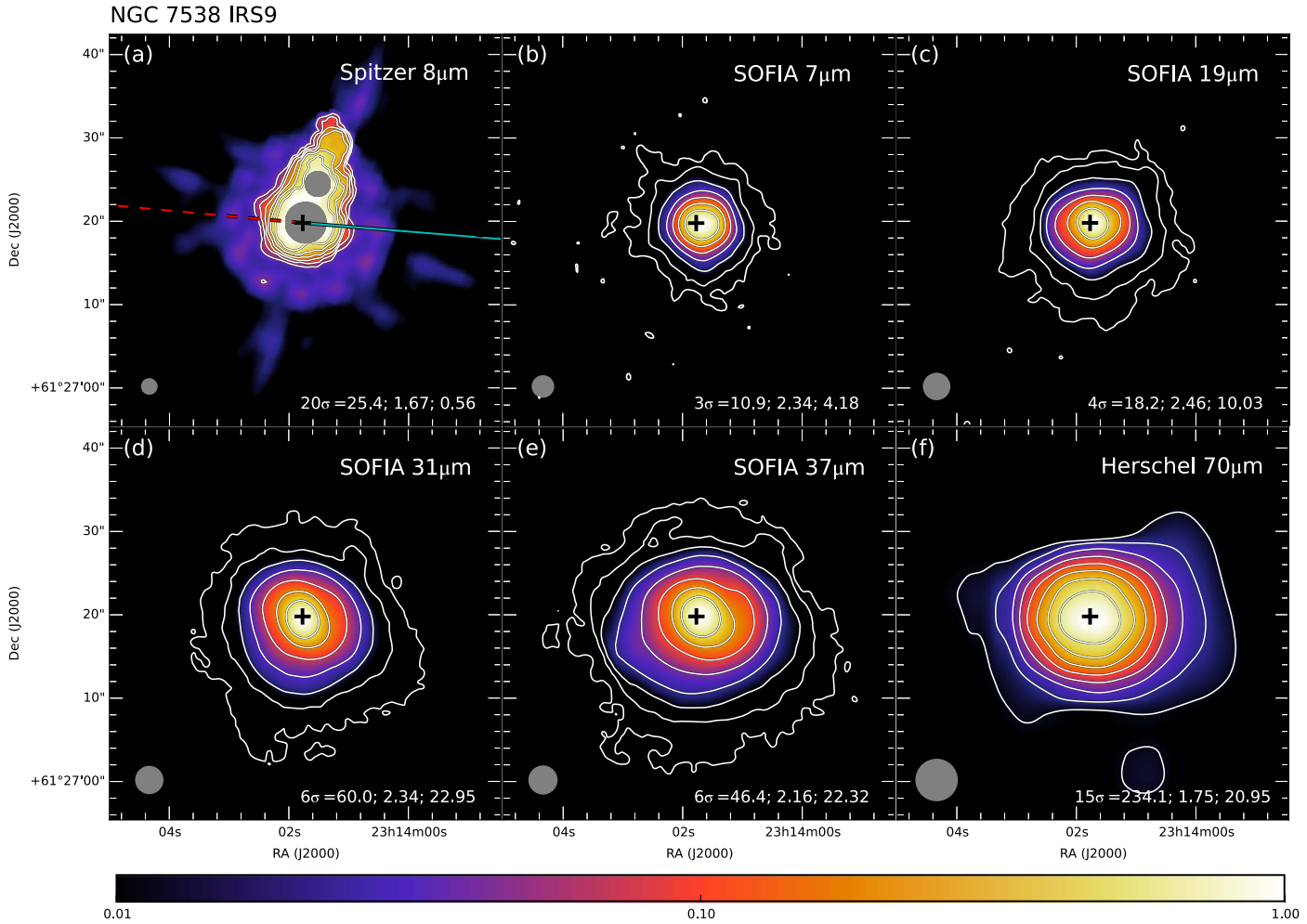

Figure 10. Multiwavelength images of NGC 7538 IRS9, following the format of Figure 1. The gray areas in panel (a) are where the source has saturated in the IRAC image. The extension to the northwest in panel (a) is a ghost, and not a real structure. The location of the 3.6 cm radio continuum peak from Sandell et al. (2005) is shown as a large cross in all panels at R.A.(J2000) = $23^{h}14^{m}01\overset{s}{.}77$, decl.(J2000) = $+61°27'19\overset{''}{.}8$. The outflow axis angle and the blueshifted outflow direction are given by the HCO^{+} observations of Sandell et al. (2005). The data used to create this figure are available.

et al. (2013a). These differences are due to our use of a fixed aperture size and geometry. Also, our SED now replaces *IRAS* fluxes with those measured by *Herschel*.

4.3.2. ZT Model Fitting Results

Figure 13 shows the results of fitting the ZT protostellar radiative transfer models to the fixed aperture, background-subtracted SEDs. Note that the data at $\lesssim 8$ μm are considered to be upper limits given that PAH emission and transiently heated small grain emission are not well treated in the models.

The parameters of the best-fit ZT models are listed in the left side of Table 3. For each source, the best five models are shown, ordered from best to worst as measured by χ^2. Note that these are distinct physical models with differing values of M_c, Σ_{cl}, and/or m_*, i.e., we do not display simple variations of θ_{view} or A_V for each of these different physical models. Recall that the models are based on the Turbulent Core Accretion theory (MT03), which links protostellar accretion rate to core mass, clump mass surface density, and evolutionary stage (i.e., the mass of the protostar, m_*). Also the core radius, R_c, is specified by M_c and Σ_{cl}. The accretion disk is always assumed to have a mass that is one-third of m_*. These models (and those of Robitaille et al., discussed below) are all for a single protostar within a core. Note that even if observed cores are shown to contain multiple sources, this approximation may still be reasonable if the primary source dominates the luminosity of the system.

In general, the best-fit models have protostellar masses m_* $\sim$ 10–50 $M_\odot$ accreting at rates of $\sim 1 \times 10^{-4}$–1×10^{-3} $M_\odot$ yr^{-1} inside cores of initial masses $M_c \sim$ 30–500 $M_\odot$ embedded in clumps with mass surface densities $\Sigma_{cl} \sim$ 0.1–3 g cm^{-2} (note that this is the full range of Σ_{cl} covered by the model grid).

In many sources, the best five models have similar values of χ^2, i.e., they are of similar goodness of fit. In these cases, among the best five models, there can also still be a significant variation in model parameters, which illustrates degeneracies that exist in trying to constrain protostellar properties from only their MIR to FIR SEDs. There are also likely to be other models beyond the best five that are still reasonable fits to the SEDs. However, we will not explore these here, since already the consideration of just the best five models shows the merits and limitations of this SED fitting.

Some of the degeneracies may be broken by using additional information. One simple check is whether the size of the protostellar core fits inside the aperture used to define the SED.

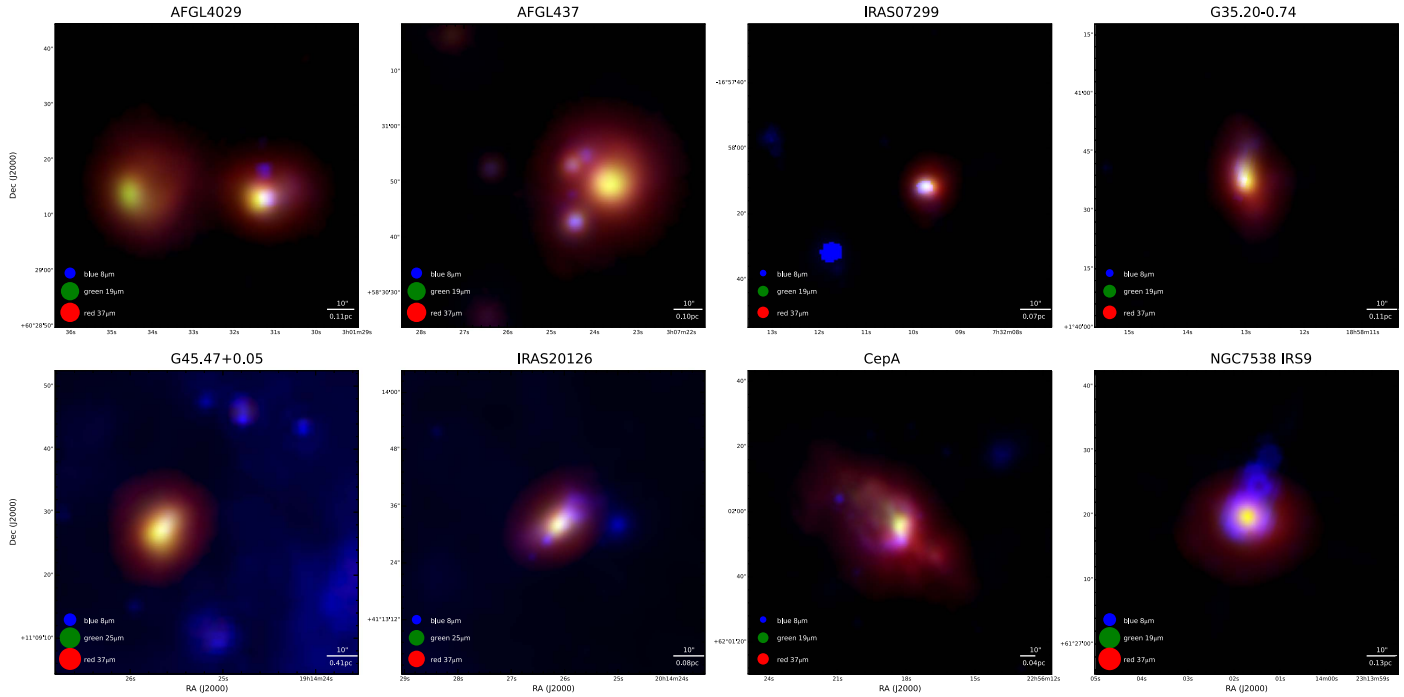

Figure 11. Gallery of RGB images of the eight protostellar sources, as labeled. The legend shows the wavelengths used and the beam sizes at these wavelengths. SOFIA-FORCAST 37 μm is always shown in red, and *Spitzer* IRAC 8 μm is always shown in blue (note this occasionally saturates in the brightest parts of some sources: see previous individual source images). Green usually shows SOFIA-FORCAST 19 μm, except for G45.47+0.05 and IRAS 20126, where it displays FORCAST 25 μm.

The most self-consistent situation is when R_c is similar to $R_{\rm ap}$. If $R_c \ll R_{\rm ap}$, then the peak of the SED is still likely to be well-measured, but the long wavelength emission from cooler material will be overestimated, i.e., the clump background subtraction would have been underestimated. If $R_c \gg R_{\rm ap}$, then the observed and model SED comparison is not self-consistent, although the peak of the SED from the warmer material may still be contained in the aperture. Better constraints come from using more detailed morphological information, e.g., MIR/FIR intensity profiles along the outflow axis (Zhang et al. 2013b). A joint fitting of SEDs and image morphologies will be carried out in a future paper in this series, following the methods of Zhang et al. (2013b). Also, associated predictions of radio continuum free–free emission (Tanaka et al. 2016) and observations of the mass of the protostellar envelope are expected to be able to break degeneracies in the models, and will be investigated in future works.

We now describe the results of the ZT SED model fitting of each of the sources, using the best five models as examples.

AFGL 4029: The best-fit model, with $\chi^2 = 1.08$, has $m_* = 12\,M_\odot$ accreting at $1.9 \times 10^{-4}\,M_\odot$ yr^{-1} from a $30\,M_\odot$ core in a $\Sigma_{\rm cl} = 1.0$ g cm^{-2} clump. Such a source has $L_{\rm bol} = 4.1 \times 10^4\,L_\odot$. However, an almost equally good model (the next best fit with $\chi^2 = 1.32$) has a protostar with $48\,M_\odot$ forming from a $160\,M_\odot$ core in a $\Sigma_{\rm cl} = 0.3$ g cm^{-2} clump, seen nearly edge-on with a much larger foreground extinction and with an almost 10× larger bolometric luminosity. This specific example illustrates the kinds of degeneracies that are present in fitting protostellar models from MIR to FIR SEDs alone, and in this case such fitting is not very constraining on the protostellar properties. However, we note that if the source aperture size information is taken into account, then the second case of a more massive, lower-density core has a radius of 17″ that is significantly larger than the aperture radius used to define the SED (11.″2). Thus, flux profile fitting may be helpful here to break model degeneracies, in particular excluding models that are too large for consistency with the size of the region used to define the SED.

AFGL 437: This source also has a best-fit model with $\chi^2 \simeq 1$. However, here the fifth best model is a significantly worse fit with $\chi^2 \simeq 2.2$. Most models involve fairly massive, $\sim$200 $M_\odot$ cores in a low $\Sigma = 0.1$ g cm^{-2} environment, but one example has a $50\,M_\odot$ core in a much higher $\Sigma = 3.2$ g cm^{-2} clump. This case also has a viewing angle that is close to the outflow cavity-opening angle so that there are high levels of shorter wavelength emission, clearly distinguishable among the SEDs.

IRAS 07299: Note that for this source, which lacks *Herschel* data, there are only four effective data points (plus the 3–8 μm data treated as upper limits) constraining the models. The values of χ^2 are small, i.e., about 0.5, for the best-fit case. These models indicate 8–16 $M_\odot$ protostars in relatively low-Σ cores viewed nearly edge-on are preferred. However, these models have core radii that can be several times larger than the aperture radius (but note that the 10–40 μm emission in these models is generally quite concentrated in the inner region of the core; ZTH14). Longer wavelength data would obviously be helpful here to break some of these degeneracies.

G35.20–0.74: Here, the analysis also yields several models with a similar goodness of fit, but now with relatively high values of $\chi^2 \simeq 2.6$. Inspection of the SEDs shows that the models struggle to match the longer wavelength fluxes, i.e., $\geqslant$160 μm, with the model fluxes too small by about a factor of 1.7 at this wavelength. These long wavelength data are sensitive to the presence of cooler material. It is possible that better model fits could be achieved if either background

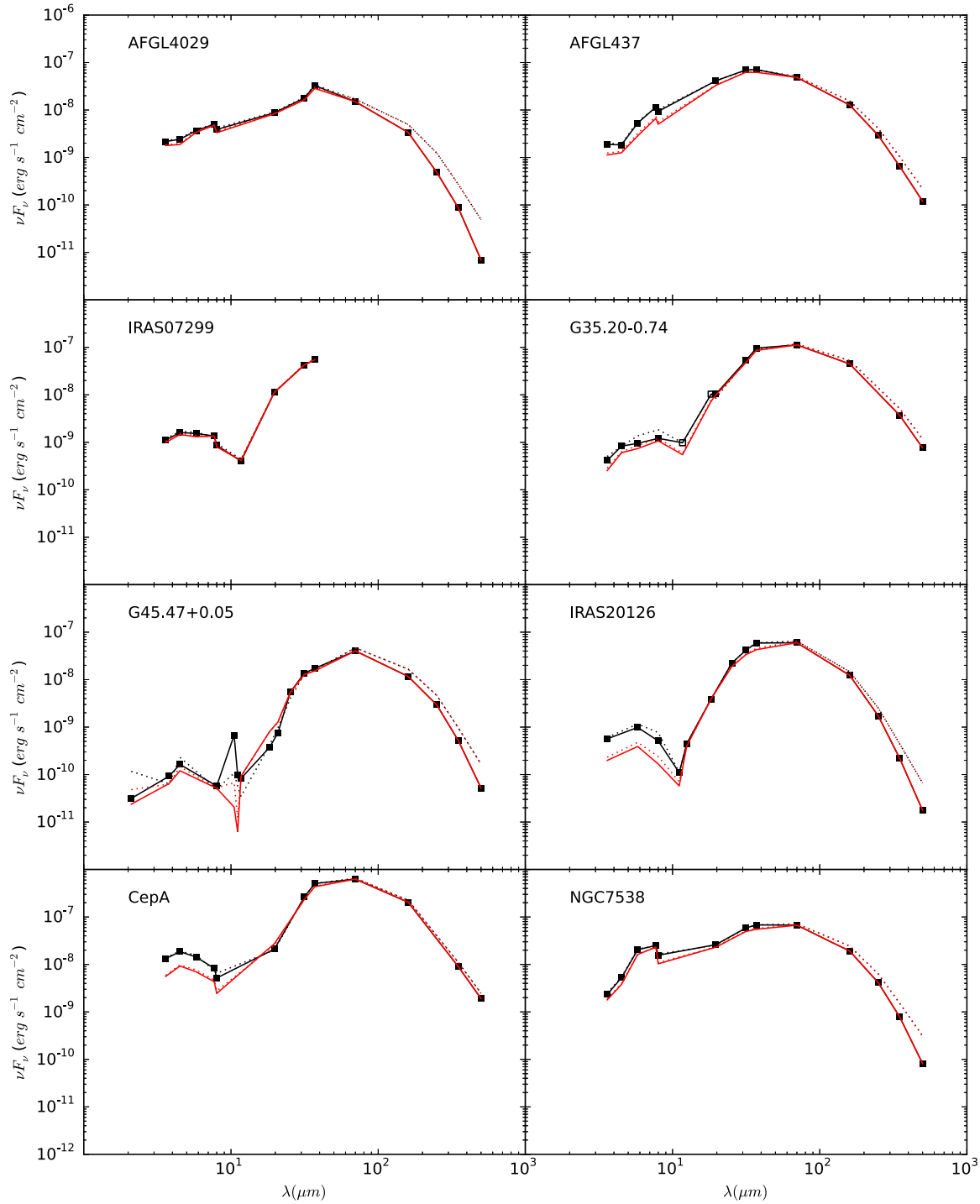

Figure 12. SEDs of the first eight sources of the SOMA Survey. Total fluxes with no background subtraction applied are shown by dotted lines. The fixed aperture case is the black dotted line; the variable aperture (at <70 μm) case is the red dotted line. The background-subtracted SEDs are shown by solid lines: black for fixed aperture (the fiducial case); red for variable aperture. Black solid squares indicate the actual measured values that sample the fiducial SED. Note that the open squares in the Gemini data of G35.20–0.74 are values where no background subtraction could be done given the limited field of view of the observations.

subtraction has been underestimated and/or if the defined aperture radius is too large and includes too much surrounding clump material. Other possibilities are that for this source the approximation of there being a single dominant source of luminosity is not as valid as in other cases, which makes the model fits be of generally poorer quality. As discussed in Section 4.1.4, there is evidence for G35.20–0.74 hosting a binary system. Considering the results of the model fitting, there appears to be a dichotomy among the best models, with higher-mass cores in low-Σ_{cl} clumps and lower-mass cores (but still $\sim$100 $M_\odot$) in high-Σ_{cl} clumps giving similar values of χ^2. However, a more intermediate case of a 200 $M_\odot$ core in a $\Sigma_{cl} = 0.3$ g cm^{-2} clump environment is also possible. Again, these results illustrate the types of degeneracies that are present when trying to constrain protostellar properties from such SED fitting. We note that most of these models are in a relatively

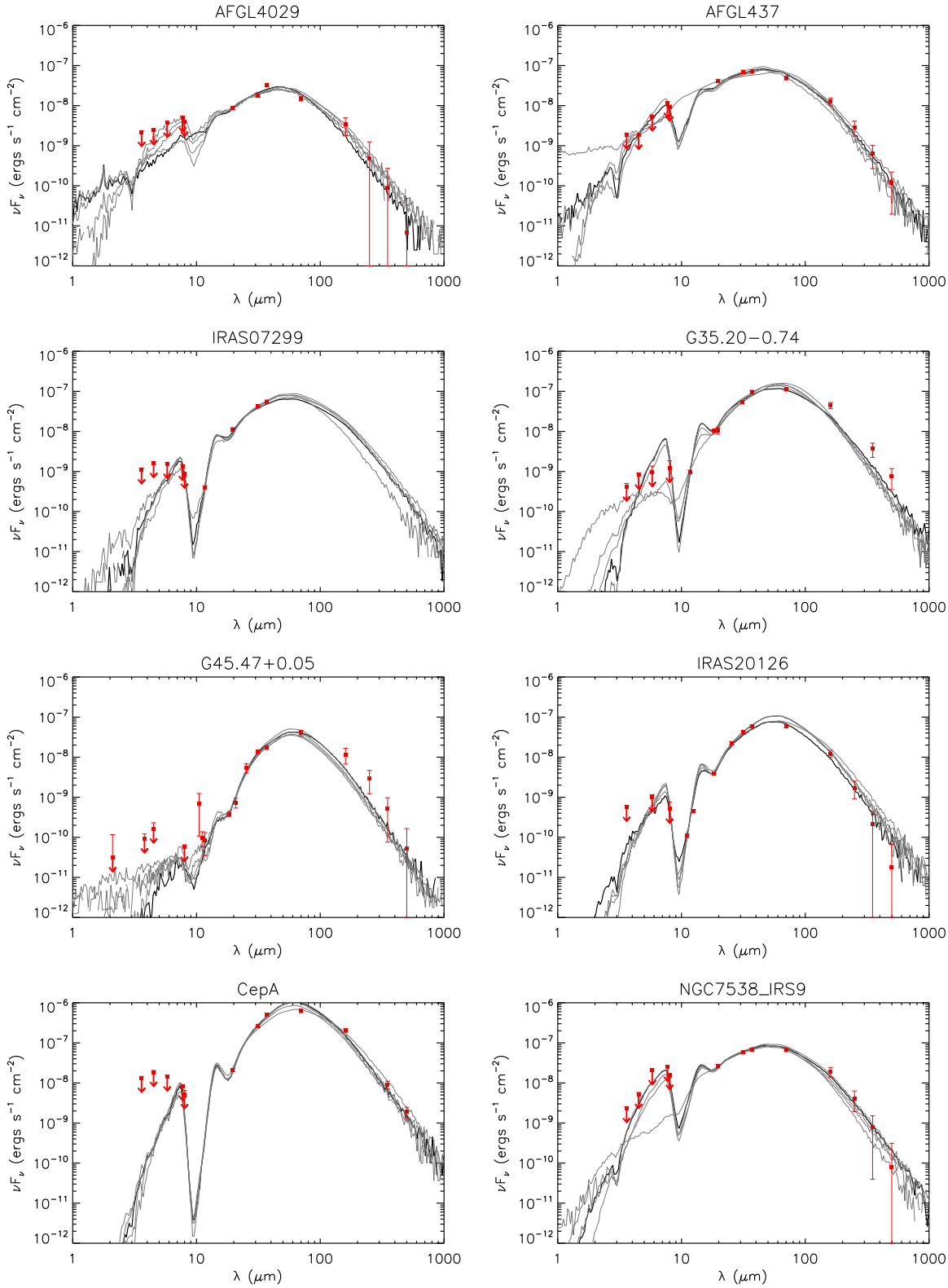

Figure 13. Protostar model fitting to the fixed aperture, background-subtracted SED data using the ZT model grid. For each source, the best-fit model is shown with a solid black line and the next four best models are shown with solid gray lines. Flux values are those from Table 2. Note that the data at $\lesssim$8 μm are treated as upper limits (see text). The resulting model parameter results are listed in Table 3.

early stage of formation, so the opening angles of their outflow cavities are quite narrow, i.e., ∼20°, and such angles are quite similar to those implied by the morphologies shown by the high-resolution 11 and 18 μm images of the source presented by De Buizer (2006); see also Zhang et al. (2013a).

G45.47+0.05: For this source, the best-fit model has $\chi^2 \simeq 1.2$, with the fifth best model having a value of 1.7. The best two preferred models have a similar goodness of fit and involve a 200–300 $M_\odot$ core in a high-Σ_{cl} clump with a current protostellar mass of ∼30–50 $M_\odot$ viewed nearly

Table 3
Parameters of the Five Best-fitted Models of Zhang & Tan and Robitaille et al.

Source	Zhang & Tan Models											Robitaille et al. Models									
	χ^2	M_c ($M_\odot$)	Σ_{cl} (g cm^{-2})	R_c (pc) ($''$)	m_* ($M_\odot$)	θ_{view} (°)	A_V (mag)	M_{env} ($M_\odot$)	$\theta_{w,esc}$ (°)	$\dot{M}_{disk}$ ($M_\odot$ yr^{-1})	L_{bol} ($L_\odot$)	χ^2	m_* ($M_\odot$)	θ_{view} (°)	A_V (mag)	M_{env} ($M_\odot$)	R_{env} (pc) ($''$)	$\theta_{w,esc}$ (°)	$\dot{M}_{env}$ ($M_\odot$ yr^{-1})	$\dot{M}_{disk}$ ($M_\odot$ yr^{-1})	L_{bol} ($L_\odot$)
AFGL 4029	1.08	30	1.0	0.04 (4)	12	65	2.0	6	53	1.9(−4)	4.1(4)	1.79	12	57	62.3	58	0.34 (36)	36	2.0(−4)	5.8(−8)	1.0(4)
$d = 2.0$ kpc	1.32	160	0.3	0.17 (17)	48	86	23.2	14	77	1.1(−4)	3.4(5)	1.79	12	87	46.9	83	0.48 (50)	34	1.7(−4)	1.8(−6)	1.1(4)
$R_{ap} = 11\farcs2$	1.33	80	0.1	0.21 (21)	12	77	2.0	47	40	5.4(−5)	1.6(4)	1.80	11	18	45.8	79	0.31 (32)	44	3.9(−4)	8.7(−9)	9.1(3)
	1.52	60	0.3	0.10 (10)	16	62	4.0	19	56	1.1(−4)	3.6(4)	1.81	13	63	56.3	69	0.48 (50)	42	1.7(−4)	4.4(−7)	1.2(4)
	1.53	50	0.3	0.09 (10)	12	55	1.0	22	46	1.0(−4)	2.4(4)	1.81	14	49	53.0	66	0.48 (49)	20	1.1(−4)	1.6(−8)	8.8(3)
AFGL 437	0.91	160	0.1	0.29 (30)	16	58	0.0	116	32	8.1(−5)	3.3(4)	0.79	15	87	15.7	124	0.48 (50)	35	2.9(−4)	9.7(−6)	2.3(4)
$d = 2.0$ kpc	1.48	160	0.1	0.29 (30)	24	86	15.2	87	45	8.5(−5)	7.8(4)	0.83	15	81	16.3	124	0.48 (50)	35	2.9(−4)	9.7(−6)	2.3(4)
$R_{ap} = 32\farcs0$	1.55	50	3.2	0.03 (3)	8	29	0.0	35	25	6.0(−4)	1.7(4)	1.05	16	76	12.9	97	0.48 (50)	17	1.8(−4)	2.9(−4)	2.0(4)
	2.02	160	0.1	0.29 (30)	32	89	23.2	55	59	7.6(−5)	1.5(5)	1.07	14	81	10.0	141	0.48 (50)	30	2.9(−4)	3.0(−7)	1.9(4)
	2.22	200	0.1	0.33 (34)	12	34	0.0	174	20	8.0(−5)	2.0(4)	1.07	16	87	10.0	161	0.48 (50)	24	3.1(−4)	1.8(−7)	2.3(4)
IRAS 07299	0.54	240	0.1	0.36 (44)	8	86	5.1	226	13	7.1(−5)	1.1(4)	1.49	19	81	27.6	35	0.14 (17)	5	4.4(−4)	…	1.0(4)
$d = 1.68$ kpc	0.62	80	0.3	0.12 (14)	16	89	11.1	42	42	1.5(−4)	4.2(4)	1.52	19	76	28.2	35	0.14 (17)	5	4.4(−4)	…	1.0(4)
$R_{ap} = 7\farcs7$	0.86	240	0.1	0.36 (44)	12	89	49.5	211	19	8.5(−5)	2.0(4)	1.55	19	87	27.9	35	0.14 (17)	5	4.4(−4)	…	1.0(4)
	1.14	200	0.1	0.33 (40)	12	86	51.5	174	20	8.0(−5)	2.0(4)	1.58	18	87	17.0	70	0.23 (29)	7	3.8(−4)	…	8.7(3)
	1.24	400	0.1	0.47 (57)	8	62	0.0	386	10	8.2(−5)	1.0(4)	1.60	19	63	29.7	35	0.14 (17)	5	4.4(−4)	…	1.0(4)
G35.20–0.74	2.63	480	0.1	0.51 (48)	16	48	40.4	440	15	1.2(−4)	3.8(4)	2.26	20	87	20.7	597	0.48 (45)	34	1.6(−3)	2.8(−7)	4.7(4)
$d = 2.2$ kpc	2.64	100	3.2	0.04 (4)	12	29	70.7	77	20	9.4(−4)	5.2(4)	2.40	20	81	24.1	597	0.48 (45)	34	1.6(−3)	2.8(−7)	4.7(4)
$R_{ap} = 32\farcs0$	2.76	320	0.1	0.42 (39)	24	68	81.8	256	27	1.2(−4)	8.4(4)	2.49	20	76	33.0	597	0.48 (45)	34	1.6(−3)	2.8(−7)	4.7(4)
	2.76	80	3.2	0.04 (3)	12	39	15.2	58	22	8.4(−4)	5.0(4)	2.54	19	70	16.4	679	0.48 (45)	27	1.5(−3)	2.6(−7)	4.3(4)
	2.77	200	0.3	0.19 (17)	12	22	43.4	173	17	1.9(−4)	4.0(4)	2.70	18	76	16.8	560	0.48 (45)	29	1.2(−3)	3.9(−6)	3.6(4)
G45.47+0.05	1.21	200	3.2	0.06 (1)	32	86	63.6	140	25	1.7(−3)	4.6(5)	3.36	31	57	11.1	1562	0.48 (12)	20	4.1(−3)	…	1.4(5)
$d = 8.4$ kpc	1.34	320	1.0	0.13 (3)	48	89	46.5	200	35	9.3(−4)	5.1(5)	3.67	34	63	10.0	1725	0.48 (12)	19	4.7(−3)	…	1.7(5)
$R_{ap} = 14\farcs4$	1.57	320	1.0	0.13 (3)	32	68	15.2	252	24	8.2(−4)	2.7(5)	3.94	29	70	15.2	967	0.48 (12)	17	2.4(−3)	…	1.2(5)
	1.62	240	1.0	0.11 (3)	32	86	1.0	170	30	7.2(−4)	2.6(5)	3.98	29	81	10.0	967	0.48 (12)	17	2.4(−3)	…	1.2(5)
	1.75	240	1.0	0.11 (3)	24	55	0.0	192	23	6.6(−4)	1.7(5)	3.99	34	81	37.7	1008	0.48 (12)	24	2.9(−3)	…	1.7(5)
IRAS 20126	1.82	80	0.3	0.12 (15)	16	74	37.4	42	42	1.5(−4)	4.2(4)	1.10	18	76	92.4	230	0.48 (61)	17	4.4(−4)	5.7(−7)	2.3(4)
$d = 1.64$ kpc	2.07	120	0.3	0.14 (18)	24	74	69.7	57	47	1.8(−4)	9.3(4)	1.10	18	70	96.7	230	0.48 (61)	17	4.4(−4)	5.7(−7)	2.3(4)
$R_{ap} = 12\farcs8$	2.32	80	0.3	0.12 (15)	12	44	73.7	53	31	1.4(−4)	3.4(4)	1.11	18	87	89.9	230	0.48 (61)	17	4.4(−4)	5.7(−7)	2.3(4)
	2.33	200	0.1	0.33 (41)	12	86	65.7	174	20	8.0(−5)	2.0(4)	1.14	18	81	90.9	230	0.48 (61)	17	4.4(−4)	5.7(−7)	2.3(4)
	2.39	100	0.3	0.13 (16)	16	51	66.7	61	36	1.6(−4)	4.5(4)	1.26	18	70	107.9	107	0.35 (44)	13	3.2(−4)	1.0(−5)	2.4(4)
Cep A	2.23	160	0.3	0.17 (49)	16	44	94.9	125	26	2.0(−4)	5.0(4)	1.47	19	57	57.1	723	0.48 (143)	17	1.4(−3)	5.9(−5)	2.8(4)
$d = 0.70$ kpc	2.30	160	0.3	0.17 (49)	12	29	100.0	135	20	1.8(−4)	3.8(4)	1.47	19	63	47.1	723	0.48 (143)	17	1.4(−3)	5.9(−5)	2.8(4)
$R_{ap} = 48\farcs0$	2.32	480	0.1	0.51 (150)	12	83	85.9	460	12	1.1(−4)	2.4(4)	1.48	19	70	40.1	723	0.48 (143)	17	1.4(−3)	5.9(−5)	2.8(4)
	2.70	160	0.3	0.17 (49)	24	80	100.0	98	37	2.2(−4)	9.9(4)	1.49	19	49	73.3	723	0.48 (143)	17	1.4(−3)	5.9(−5)	2.8(4)
	3.04	120	0.3	0.14 (42)	12	48	73.7	93	24	1.6(−4)	3.6(4)	1.50	17	63	26.5	786	0.48 (143)	15	1.5(−3)	4.2(−6)	2.6(4)
NGC 7538	0.15	400	0.1	0.47 (36)	16	22	23.2	364	17	1.1(−4)	3.8(4)	0.36	18	18	36.2	635	0.48 (38)	10	1.2(−3)	1.4(−7)	2.3(4)
IRS9	0.19	320	0.1	0.42 (32)	16	39	2.0	281	19	1.1(−4)	3.7(4)	0.37	13	18	39.8	615	0.44 (34)	13	1.1(−3)	9.0(−6)	2.2(4)
$d = 2.65$ kpc	0.35	240	0.1	0.36 (28)	24	39	52.5	171	33	1.1(−4)	8.2(4)	0.37	13	18	37.4	622	0.48 (38)	11	9.9(−4)	4.3(−6)	2.2(4)
$R_{ap} = 25\farcs6$	0.47	480	0.1	0.51 (40)	16	22	17.2	440	15	1.2(−4)	3.8(4)	0.38	16	18	44.1	582	0.48 (38)	18	1.1(−3)	1.3(−7)	2.3(4)
	0.54	60	3.2	0.03 (2)	12	34	22.2	38	27	7.6(−4)	5.0(4)	0.40	16	18	46.5	592	0.48 (38)	22	1.1(−3)	7.5(−7)	2.6(4)

(This table is available in machine-readable form.)

edge-on. More intermediate viewing angles are returned for the next best models (and also recall we have not fully explored the full range of viewing angles that allowed for a given physical model).

IRAS 20126: Here, the best-fit value of $\chi^2 \simeq 2$. The models prefer a lower $\Sigma_{\rm cl} \lesssim 0.3\,{\rm g\,cm^{-2}}$ clump environment with a ~100–200 $M_\odot$ core that has formed a protostar with $m_* \sim$ 12–24 $M_\odot$ viewed at relatively large angles with respect to the outflow axis, i.e., with the line of sight passing through the bulk of the core infall envelope. Given the results of Chen et al. (2016), which favor a 12 $M_\odot$ protostar from the kinematics of CH_3CN that may be tracing the accretion disk, the third and fourth best-fit models may be the most applicable in this case.

Cep A: This protostar also has best-fit models with $\chi^2 \simeq 2.2$, which rise to about 3 by the fifth model. The best two models prefer $\Sigma_{\rm cl} = 0.3\ {\rm g\,cm^{-2}}$ with $M_c = 160\,M_\odot$ and $m_* = 16$ or 12 $M_\odot$ viewed at angles of 44°–29° with about 100 mag of foreground extinction.

NGC 7538 IRS9: This source has an SED that is very well fit by the ZT RT models, with $\chi^2 \simeq 0.15$ for the best case, rising to 0.5 for the fifth best physical model. Most of the models prefer $\Sigma_{\rm cl} = 0.1\,{\rm g\,cm^{-2}}$. The best-fit model has a 400 $M_\odot$ core with a 16 $M_\odot$ protostar, viewed at a relatively small angle with respect to the outflow axis, i.e., the line of sight passes close to the ouflow cavity boundary, avoiding most of the infall envelope. The SEDs of such models are relatively flat from ~20 to ~100 μm. We note that the small viewing angle of 22° of the best-fit model is similar to the value of ~20° inferred from the HCO^+ outflow by Sandell et al. (2005; see Section 4.1.8).

4.3.3. Robitaille et al. Model Fitting Results

In Figure 14, we show the results of fitting the Robitaille et al. (2007) models to the fiducial SEDs. The parameters of the best five models are also shown in the right side of Table 3. The values of χ^2 for the Robitaille et al. models are quite similar to those of the ZT models, with a modest tendency to return slightly poorer fits, even though the sampling in some parameters, like m_*, is finer than the ZT model grid and the ZT models involve fewer free parameters.

With the Robitaille et al. models, a common occurrence is that the disk accretion rates are much lower than in the ZT models, often ~100× smaller (and occasionally ~10^3× smaller). In some cases, the models do not require any disk component (indicated by "..." in the tabulated accretion rates). The envelope infall rate is always much larger than the disk accretion rate, so the models are not physically self-consistent, at least in the context of having a steadily accreting system. Lower disk accretion rates mean a smaller bolometric luminosity and so to compensate the Robitaille et al. results can involve larger protostellar masses than the ZT models, e.g., in the cases of IRAS 07299, G35.20–0.74, Cep A, or smaller overall extinctions due to lower column density cores and/or more face-on viewing angles.

The outer core envelope radii, $R_{\rm env}$, are also typically quite large, i.e., ~0.5 pc. Only for the distant source G45.47 +0.05 are these smaller than the aperture size used to define the SED. In the other sources, $R_{\rm env} > R_{\rm ap}$, sometimes by factors of five or so. Thus, most of these models are not internally self-consistent with the observations.

Considering the particular case of G35.20–0.74 is instructive. As with the ZT models, the best-fit Robitaille et al. models underpredict at long wavelengths and (slightly) overpredict near the peak of the SED. A protostellar mass of $m_* = 20\,M_\odot$ is estimated, but with a disk accretion rate of only $2.8 \times 10^{-7}\,M_\odot\,{\rm yr^{-1}}$ (so accretion power is negligible). On the other hand, the envelope mass infall rate is $1.6 \times 10^{-3}\,M_\odot\,{\rm yr^{-1}}$. The viewing angle is found to be 87°, so that the outflow axis would be close to the plane of the sky, which is very different from the result of the best ZT model. Such a geometry would not be expected to lead to strong asymmetries in the MIR/FIR morphologies of the blue- and redshifted outflow cavities.

As discussed below, future studies that use additional constraints such as observations of the radio continuum flux (which is sensitive to protostellar mass), MIR–FIR image intensity profiles along and transverse to the outflow cavity axis (which help measure the density and temperature structure of the core infall envelope and outflow), along with other tracers of the gas content, can help test between the relative validity among the Robitaille et al. models and in comparison to the ZT models.

4.4. Discussion

The above considerations illustrate current capabilities, including difficulties and uncertainties, of determining protostellar properties from simple SED fitting methods. We consider the results of the ZT model fitting to be more reliable since the models are designed with the typical expected properties of massive protostars in mind and they yield results that are internally self-consistent both physically (i.e., accretion rates through the disk are directly related to infall rates in the core envelopes; such high disk accretion rates are likely to be needed to drive powerful outflows) and observationally (i.e., the cores are more compact and are generally a better match to the aperture sizes used to define the SEDs).

Future work can help test the models further. For example, the estimated disk accretion rates can be compared with observed mass outflow rates to see if they are consistent with theoretical models of disk winds and/or X-winds (e.g., Caratti O Garatti et al. 2015; Beltrán & de Wit 2016). The model and observed image intensity profiles along and transverse to the outflow axis can be compared to better constrain the outflow opening angle and orientation (i.e., $\theta_{\rm view}$; e.g., Zhang et al. 2013b). The latter can also be compared to that estimated from a study of the kinematics of the outflowing gas. Predictions for internal density and temperature structures within the core can be tested with higher angular resolution observations, e.g., of MIR emission (e.g., Boley et al. 2013), of sub-millimeter/millimeter dust continuum (e.g., Beuther et al. 2013), and with specific temperature diagnostics such as NH_3 inversion transitions (e.g., Wang et al. 2012). Kinematics of core envelope infall (e.g., Wyrowski et al. 2016) and disk rotation (e.g., Sánchez-Monge et al. 2013) can also be probed with molecular lines. Magnetic field structures around the protostars can be inferred from observations of polarized dust continuum emission (e.g., Girart et al. 2009; Zhang et al. 2014a). The density and temperature structures of the radiative transfer models, along with their evolutionary histories, provide a framework for developing and testing astrochemical models of core envelopes, disks, and outflows (e.g., Doty et al. 2006; Drozdovskaya et al. 2014; Zhang & Tan 2015), and radio continuum emission tracing, e.g., photoionized gas, can be

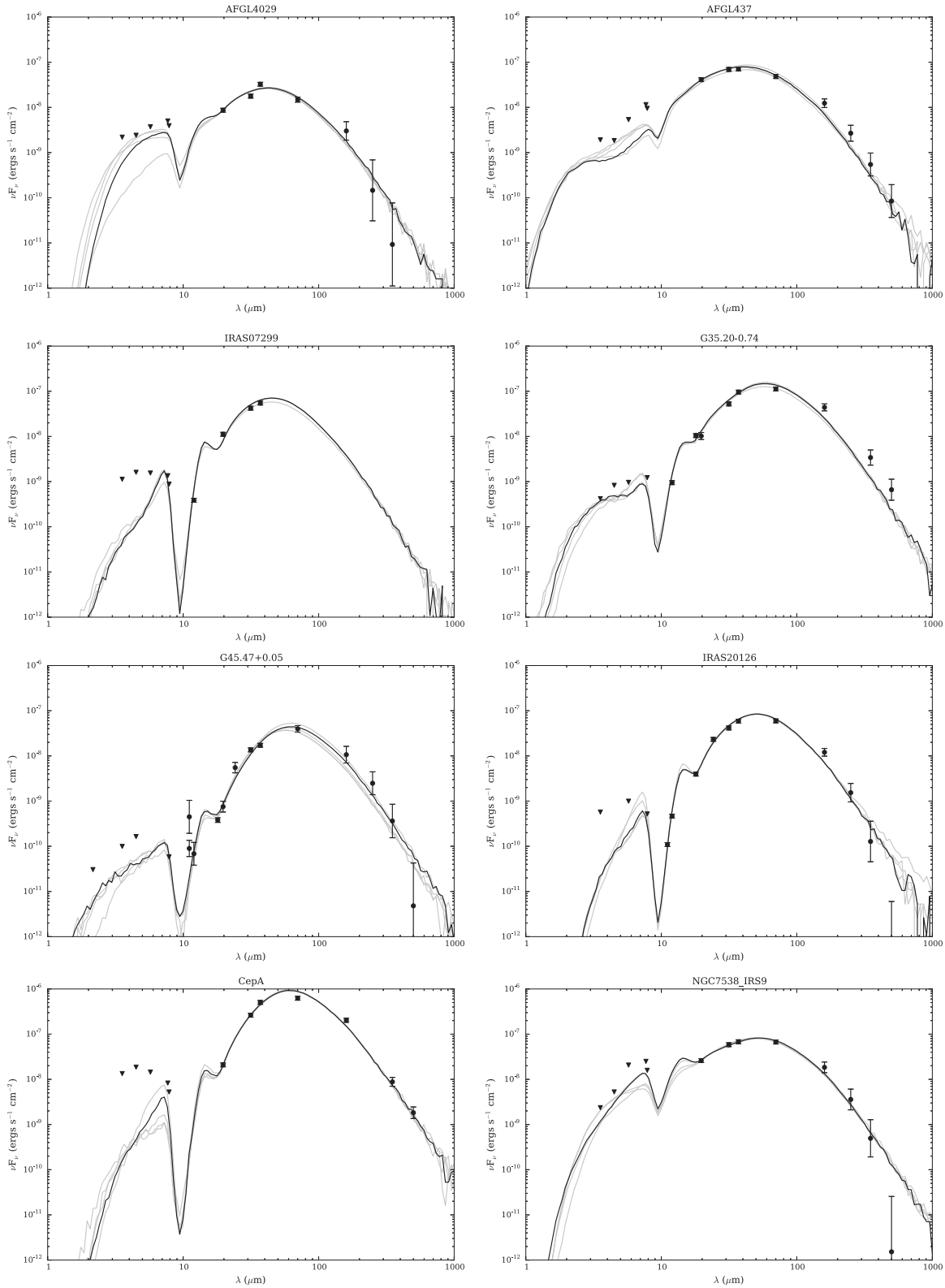

Figure 14. Protostar model fitting to the fixed aperture, background-subtracted SED data using the Robitaille et al. (2007) model grid. For each source, the best-fit model is shown with a solid black line and the next four best models are shown with solid gray lines. Flux values are those from Table 2. Note that the data at $\lesssim$8 μm are treated as upper limits (see text). Also, the fitting method sets the data point to be at the middle of the error bar range. The resulting model parameter results are listed in Table 3.

searched for (e.g., Rosero et al. 2016) and compared to theoretical predictions (e.g., Tanaka et al. 2016).

By eventually studying a large sample of protostars spanning a range of environments, masses, and evolutionary stages, we hope to discern general trends in star formation activity. For example, do protostars in higher Σ_{cl} clump environments have higher accretion rates, as would be predicted by the Turbulent Core Model? Or do such environments involve protostars

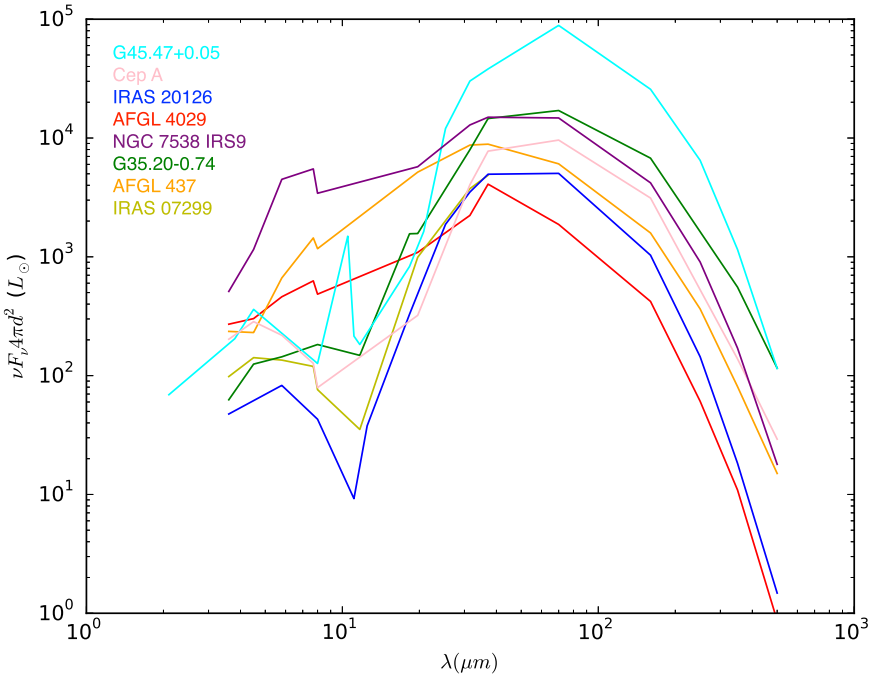

Figure 15. Bolometric flux-weighted SEDs of the eight SOMA protostars analyzed in this paper. The ordering of the legend is from high to low ZT best-fit model luminosity (top to bottom).

forming with different accretion mechanisms? Are there systematic trends in SED shape with clump environment, core mass, protostellar mass or luminosity?

As a first step in such directions, in Figure 15 we show the bolometric luminosity SEDs of the eight protostars, i.e., the νF_ν SEDs have been scaled by $4\pi d^2$, so that the height of the curves gives an indication of the luminosity of the sources, assuming isotropic emission. This figure allows one to visualize the range in luminosities present in the sample, along with any potential trends in SED shape. However, on inspecting the distributions, we do not perceive any obvious trends in SED shape with luminosity, although this is perhaps not so surprising given the current sample size.

We can compare the ordering of the vertical height of these distributions with the rank ordering of the predicted true luminosity of the protostars from the best-fit ZT models (the legend in Figure 15 lists the sources in order of decreasing ZT model luminosity). There is some, but not perfect, correspondence with the flux ordering seen in the figure. Differences are most likely due to varying levels of foreground extinction, local extinction in the core envelope (e.g., AFGL 4029's formal best-fit ZT model has a relatively low envelope mass and wide outflow cavity, so a large fraction of its luminosity would not be re-radiated in the MIR to FIR) and anisotropic beaming (i.e., the "flashlight effect," Yorke & Bodenheimer 1999). The latter effect likely boosts NGC 7538 IRS 9's apparent bolometric luminosity SED compared to that expected based on its intrinsic bolometric luminosity. Such non-intrinsic effects illustrate the need for larger samples of protostars, i.e., eventually, statistically significant samples will be required as a function of environment, mass, and evolutionary stage. This is the eventual goal of the SOMA Survey.

5. Conclusions

We have presented an overview and first results of the SOMA Star Formation Survey. The survey's scientific rationale is to test predictions of Core Accretion models of massive star formation, specifically the MIR to FIR thermal dust emission, including the influence of outflow cavities. We have presented results for the first eight sources observed in the survey. These tend to show extended MIR and FIR emission that aligns with known outflows, and being brighter on the near-facing, blueshifted side, which are predictions of Core Accretion models that involve high mass surface density cores. In principle, unrelated foreground extinction could mimic these results, but the consistency of the observed multiwavelength morphologies in the sample provides strong support for the Core Accretion scenario.

Global SEDs have been constructed and the effects of choices of aperture definition and background subtraction investigated. Our fiducial method is an SED derived from a fixed aperture and including an estimate of background subtraction, i.e., the emission from the surrounding clump environment.

These SEDs have been used to constrain properties of the protostars by comparing with theoretical radiative transfer models of massive star formation via the Turbulent Core Accretion model. These yield protostellar masses $m_* \sim 10$–$50\,M_\odot$ accreting at rates of $\sim 1 \times 10^{-4}$–$1 \times 10^{-3}\,M_\odot\,\mathrm{yr}^{-1}$ inside cores of initial masses $M_c \sim 30$–$500\,M_\odot$ embedded in clumps with mass surface densities $\Sigma_{\rm cl} \sim 0.1$–$3\,\mathrm{g\,cm}^{-2}$. We note that these are results from using a model grid with a relatively coarse sampling of initial core masses and clump envelope mass surface densities, yet quite reasonable fits are found. The derived accretion rates are comparable to the values estimated by other means, e.g., via observed infall rates in core envelopes (e.g., Wyrowski et al. 2016) and via mass outflow rates (e.g., Beltrán & de Wit 2016). However, there can be significant degeneracies in the parameters of models that provide good fits to the SEDs. Breaking these degeneracies will require additional observational contraints, such as using predictions of image intensity profiles

(e.g., Zhang et al. 2013b) or radio continuum emission that traces ionized gas (e.g., Tanaka et al. 2016).

Comparison with the widely used Robitaille et al. (2007) model grid finds large differences, especially in the derived disk accretion rates. We suspect that these differences are due, at least in part, to there being a wider choice of free parameters in the Robitaille et al. grid, which can lead to models that we consider less physically realistic, i.e., high mass infall rates in the core envelope but small disk accretion rates.

Finally, we emphasize the importance that SOFIA-FORCAST observations in the wavelength range $\sim$10–40 μm have for constraining the theoretical models. In combination with *Herschel* 70–500 μm data, they allow measurement of the thermal emission that defines the peak of the SED and probes the bulk of the bolometric flux. We consider this thermal emission simpler to model than that at shorter wavelengths, $\lesssim$8 μm, which is more affected by emission from PAHs and transiently heated small dust grains.

Future papers in this series will present additional sources, especially probing a wider range of environmental conditions, evolutionary stages, and protostellar core masses. Additional analysis that examines and models flux profiles along outflow cavity axes will be carried out, following methods developed by Zhang et al. (2013a). Ancillary observations that trace the outflowing gas will also be presented.

We thank an anonymous referee for helpful comments, which improved the manuscript. J.C.T. acknowledges several NASA-USRA-SOFIA grants that supported this research. This work is based in part on observations made with the NASA/DLR Stratospheric Observatory for Infrared Astronomy (SOFIA). This work is also based in part on observations made with the *Spitzer Space Telescope*, which is operated by the Jet Propulsion Laboratory, California Institute of Technology under a contract with NASA. This work is additionally based on observations obtained at the Gemini Observatory (program GS-2005B-Q-39), which is operated by the Association of Universities for Research in Astronomy, Inc., under a cooperative agreement with the NSF on behalf of the Gemini partnership: the National Science Foundation (United States), the National Research Council (Canada), CONICYT (Chile), Ministerio de Ciencia, Tecnologa e Innovacin Productiva (Argentina), and Ministrio da Cincia, Tecnologia e Inovao (Brazil). The lead authors were also Visiting Astronomers at the *I*nfrared Telescope Facility, which is operated by the University of Hawaii under contract NNH14CK55B with the National Aeronautics and Space Administration. The lead author was also a Visiting Astronomer.

Facilities: SOFIA (FORCAST), *Herschel* (PACS, SPIRE), *Spitzer* (IRAC), Gemini (T-ReCS, MICHELLE); IRTF (NSFCam, MIRLIN).

References

Arquilla, R., & Goldsmith, P. F. 1984, ApJ, 279, 664
Bally, J., & Lane, A. P. 1990, in ASP Conf. Ser. 14, Astrophysics with Infrared Arrays, ed. R. Elston (San Francisco, CA: ASP), 273
Bally, J., & Zinnecker, H. 2005, AJ, 129, 2281
Barentine, J. C., & Lacy, J. H. 2012, ApJ, 757, 111
Beichman, C. A. 1979, PhD thesis, Hawaii University
Beltrán, M. T., Cesaroni, R., Moscadelli, L., et al. 2016, A&A, 593, A49
Beltrán, M. T., & de Wit, W. J. 2016, A&ARv, 24, 6
Beuther, H., Linz, H., & Henning, Th. 2013, A&A, 558, 81
Beuther, H., Schilke, P., Sridharan, T. K., et al. 2002, A&A, 383, 892
Birks, J. R., Fuller, G. A., & Gibb, A. G. 2006, A&A, 458, 181
Blandford, R. D., & Payne, D. G. 1982, MNRAS, 199, 883
Boley, P. A., Linz, H., van Boeckel, R., et al. 2013, A&A, 558, A24
Bonnell, I. A., Bate, M. R., Clarke, C. J., & Pringle, J. E. 2001, MNRAS, 323, 785
Bonnell, I. A., Bate, M. R., & Zinnecker, H. 1998, MNRAS, 298, 93
Brown, A. T., Little, L. T., MacDonald, G. H., & Matheson, D. N. 1982, MNRAS, 201, 121
Butler, M. J., & Tan, J. C. 2012, ApJ, 754, 5
Caratti O Garatti, A., Stecklum, B., Garcia Lopez, R., et al. 2016, NatPh, 13, 276
Caratti O Garatti, A., Stecklum, B., Linz, H., et al. 2015, A&A, 573, A82
Casement, L. S., & McLean, I. S. 1996, ApJ, 462, 797
Cesaroni, R., Felli, M., Jenness, T., et al. 1999, A&A, 345, 949
Cesaroni, R., Felli, M., Testi, L., Walmsley, C. M., & Olmi, L. 1997, A&A, 325, 725
Cesaroni, R., Massi, F., Arcidiacono, C., et al. 2013, A&A, 549, 146
Cesaroni, R., Neri, R., Olmi, L., et al. 2005, A&A, 434, 1039
Chen, H.-R. V., Keto, E., Zhang, Q., et al. 2016, ApJ, 823, 125
Contreras Peña, C., Lucas, P. W., Kurtev, R., et al. 2017, MNRAS, 465, 3039
Cunningham, N. J., Moeckel, N., & Bally, J. 2009, ApJ, 692, 943
Cyganowski, C. J., Whitney, B. A., Holden, E., et al. 2008, AJ, 136, 2391
De Buizer, J. M. 2003, MNRAS, 341, 277
De Buizer, J. M. 2006, ApJL, 642, L57
De Buizer, J. M. 2007, ApJL, 654, L147
De Buizer, J. M., & Fisher, R. S. 2005, in High Resolution Infrared Spectroscopy in Astronomy, ed. H. U. Kaufl, R. Siebenmorgen, & A. Moorwood (Berlin: Springer), 84
De Buizer, J. M., Radomski, J. T., Telesco, C. M., & Piña, R. K. 2005, ApJS, 156, 179
De Buizer, J. M., & Vacca, W. D. 2010, AJ, 140, 196
de Wit, W. J., Hoare, M. G., Fujiyoshi, T., et al. 2009, A&A, 494, 157
Deharveng, L., Zavagno, A., Anderson, L. D., et al. 2012, A&A, 546, A74
Deharveng, L., Zavagno, A., Cruz-Gonzalez, I., et al. 1997, A&A, 317, 459
Dent, W. R. F., Little, L. T., Kaifu, N., Ohishi, M., & Suzuki, S. 1985a, A&A, 146, 375
Dent, W. R. F., Little, L. T., Sato, S., Ohishi, M., & Yamashita, T. 1985b, MNRAS, 217, 217
Dent, W. R. F., Sandell, G., Duncan, W. D., & Robson, E. I. 1989, MNRAS, 238, 1497
Doty, S. D., van Dishoeck, E. F., & Tan, J. C. 2006, A&A, 454, L5
Drozdovskaya, M. N., Walsh, C., Visser, R., Harsono, D., & van Dishoeck, E. F. 2014, MNRAS, 445, 913
Dzib, S., Loinard, L., Rodríguez, L. F., et al. 2011, ApJ, 733, 71
Fazio, G. G., Hora, J. L., Allen, L. E., et al. 2004, ApJS, 154, 10
Fich, M., & Blitz, L. 1984, ApJ, 279, 125
Forster, J. R., & Caswell, J. L. 1989, A&A, 213, 339
Fujisawa, K., Sugiyama, K., Motogi, K., et al. 2014, PASJ, 66, 31
Garay, G., Ramirez, S., Rodriguez, L. F., Curiel, S., & Torrelles, J. M. 1996, ApJ, 459, 193
Gibb, A. G., Hoare, M. G., Little, L. T., & Wright, M. C. H. 2003, MNRAS, 339, 1011
Ginsburg, A., Bally, J., & Williams, J. P. 2011, MNRAS, 418, 2121
Girart, J. M., Beltrán, M. T., Zhang, Q., Rao, R., & Estalella, R. 2009, Sci, 324, 1408
Goetz, J. A., Pipher, J. L., Forrest, W. J., et al. 1998, ApJ, 504, 359
Gómez, J. F., Sargent, A. I., Torrelles, J. M., et al. 1999, ApJ, 514, 287
Gómez, J. F., Torrelles, J. M., Estalella, R., et al. 1992, ApJ, 397, 492
Goodman, A. A., Benson, P. J., Fuller, G. A., & Myers, P. C. 1993, ApJ, 406, 528
Griffin, M. J., Abergel, A., Abreu, A., et al. 2010, A&A, 518, L3
Heaton, B. D., & Little, L. T. 1988, A&A, 195, 193
Hernández-Hernández, V., Zapata, L., Kurtz, S., & Garay, G. 2014, ApJ, 786, 38
Herter, T. L., Vacca, W. D., Adams, J. D., et al. 2013, PASP, 125, 1393
Hoare, M. G., Purcell, C. R., Churchwell, E. B., et al. 2012, PASP, 124, 939
Hofner, P., Cesaroni, R., Olmi, L., et al. 2007, A&A, 465, 197
Hosokawa, T., & Omukai, K. 2009, ApJ, 691, 823
Hosokawa, T., Yorke, H. W., & Omukai, K. 2010, ApJ, 721, 478
Hughes, V. A., & Wouterloot, J. G. A. 1984, ApJ, 276, 204
Hunter, T. R., Brogan, C. L., MacLeod, G., et al. 2017, ApJL, 837, L29
Johnston, K. G., Keto, E., Robitaille, T. P., & Wood, K. 2011, MNRAS, 415, 2953
Jones, T. J., Woodward, C. E., & Kelley, M. S. 2004, AJ, 128, 2448
Keto, E., & Zhang, Q. 2010, MNRAS, 406, 102
Königl, A., & Pudritz, R. E. 2000, in Protostars and Planets IV, ed. V. Mannings (Tucson, AZ: Univ. Arizona Press), 759

Kratter, K. M., Matzner, C. D., & Krumholz, M. R. 2008, ApJ, 681, 375
Kuiper, R., Yorke, H., & Turner, N. J. 2015, ApJ, 800, 86
Kumar Dewangan, L., & Anandarao, B. G. 2010, MNRAS, 402, 2583
Kurtz, S., Churchwell, E., & Wood, D. O. S. 1994, ApJS, 91, 659
Lee, H.-T., Liao, W.-T., Froebrich, D., et al. 2013, ApJS, 208, 23
Li, J., Wang, J., Gu, Q., Zhang, Z.-Y., & Zheng, X. 2012, ApJ, 745, 47
Little, L. T., Kelly, M. L., & Murphy, B. T. 1998, MNRAS, 294, 105
Liu, T., Wu, Y.-F., & Wang, K. 2010, RAA, 10, 67
Matzner, C. D., & McKee, C. F. 2000, ApJ, 545, 364
McKee, C. F., & Tan, J. C. 2002, Natur, 416, 59
McKee, C. F., & Tan, J. C. 2003, ApJ, 585, 850
McLaughlin, D. E., & Pudritz, R. E. 1996, ApJ, 469, 194
McLaughlin, D. E., & Pudritz, R. E. 1997, ApJ, 476, 750
Meakin, C. A., Hines, D. C., & Thompson, R. I. 2005, ApJ, 634, 1146
Mitchell, G. F., & Hasegawa, T. I. 1991, ApJL, 371, L33
Moscadelli, L., Cesaroni, R., Rioja, M. J., Dodson, R., & Reid, M. J. 2011, A&A, 526, A66
Moscadelli, L., Reid, M. J., Menten, K. M., et al. 2009, ApJ, 693, 406
Narayanan, G., & Walker, C. K. 1996, ApJ, 466, 844
Ortega, M. E., Paron, S., Cichowolski, S., Rubio, M., & Dubner, G. 2012, A&A, 546, A96
Ossenkopf, V., & Henning, T. 1994, A&A, 291, 943
Palau, A., Fuente, A., Girart, J. M., et al. 2013, ApJ, 762, 120
Paron, S., Fariña, C., & Ortega, M. E. 2013, A&A, 559, L2
Pilbratt, G. L., Riedinger, J. R., Passvogel, T., et al. 2010, A&A, 518, L1
Poglitsch, A., Waelkens, C., Geis, N., et al. 2010, A&A, 518, L2
Qin, S.-L., Wang, J.-J., Zhao, G., Miller, M., & Zhao, J.-H. 2008, A&A, 484, 361
Qiu, K., Zhang, Q., Menten, K. M., Liu, H. B., & Tang, Y.-W. 2013, ApJ, 779, 182
Ray, T. P., Poetzel, R., Solf, J., & Mundt, R. 1990, ApJL, 357, L45
Reid, M. J., Menten, K. M., Zheng, X. W., et al. 2009, ApJ, 700, 137
Ressler, M. E., Werner, M. W., Van Cleve, J., & Chou, H. A. 1994, ExA, 3, 277
Robitaille, T. P., Whitney, B. A., Indebetouw, R., & Wood, K. 2007, ApJS, 169, 328
Rodriguez, L. F., Ho, P. T. P., & Moran, J. M. 1980, ApJL, 240, L149
Rosero, V., Hofner, P., Claussen, M., et al. 2016, ApJS, 227, 25
Sánchez-Monge, Á., Beltrán, M. T., Cesaroni, R., et al. 2014, A&A, 569, A11
Sánchez-Monge, Á., Cesaroni, R., Beltrán, M. T., et al. 2013, A&A, 552, L10
Sandell, G., Goss, W. M., & Wright, M. 2005, ApJ, 621, 839
Shakura, N. I., & Sunyaev, R. A. 1973, A&A, 24, 337
Shepherd, D. S., & Churchwell, E. 1996, ApJ, 457, 267
Shu, F. H. 1977, ApJ, 214, 488
Shu, F. H., Najita, J. R., Shang, H., & Li, Z.-Y. 2000, in Protostars and Planets IV, ed. V. Mannings (Tucson, AZ: Univ. Arizona Press), 789
Shure, M. A., Toomey, D. W., Rayner, J. T., Onaka, P. M., & Denault, A. J. 1994, Proc. SPIE, 2198, 614
Su, Y.-N., Liu, S.-Y., Chen, H.-R., Zhang, Q., & Cesaroni, R. 2007, ApJ, 671, 571
Tan, J. C., Beltrán, M. T., Caselli, P., et al. 2014, in Protostars and Planets VI, ed. H. Beuther et al. (Tucson, AZ: Univ. Arizona Press), 149
Tan, J. C., Kong, S., Zhang, Y., et al. 2016, ApJL, 821, L3
Tanaka, K. E. I., Tan, J. C., & Zhang, Y. 2016, ApJ, 818, 1
Torrelles, J. M., Gomez, J. F., Anglada, G., et al. 1992, ApJ, 392, 616
Torrelles, J. M., Verdes-Montenegro, L., Ho, P. T. P., Rodriguez, L. F., & Canto, J. 1993, ApJ, 410, 202
Ulrich, R. K. 1976, ApJ, 210, 377
Walsh, A. J., Bertoldi, F., Burton, M. G., & Nikola, T. 2001, MNRAS, 326, 36
Walsh, A. J., Burton, M. G., Hyland, A. R., & Robinson, G. 1998, MNRAS, 301, 640
Walsh, A. J., Burton, M. G., Hyland, A. R., & Robinson, G. 1999, MNRAS, 309, 905
Wang, Ke., Zhang, Q., Wu, Y., Li, H.-B., & Zhang, H. 2012, ApJL, 745, L30
Wang, P., Li, Z.-Y., Abel, T., & Nakamura, F. 2010, ApJ, 709, 27
Weintraub, D. A., & Kastner, J. H. 1996, ApJ, 458, 670
Werner, M. W., Becklin, E. E., Gatley, I., et al. 1979, MNRAS, 188, 463
White, R. L., Becker, R. H., & Helfand, D. J. 2005, AJ, 130, 586
Whitney, B. A., Robitaille, T. P., Bjorkman, J. E., et al. 2013, ApJS, 207, 30
Whitney, B. A., Wood, K., Bjorkman, J. E., & Wolff, M. J. 2003, ApJ, 591, 1049
Wilner, D. J., Ho, P. T. P., & Zhang, Q. 1996, ApJ, 462, 339
Wood, D. O. S., & Churchwell, E. 1989, ApJS, 69, 831
Wu, Y., Zhang, Q., Chen, H., et al. 2005, AJ, 129, 330
Wu, Y. W., Sato, M., Reid, M. J., et al. 2014, A&A, 566, A17
Wynn-Williams, C. G., Becklin, E. E., Beichman, C. A., Capps, R., & Shakeshaft, J. R. 1981, ApJ, 246, 801
Wynn-Williams, C. G., Becklin, E. E., & Neugebauer, G. 1974, ApJ, 187, 473
Wyrowski, F., Güsten, R., Menten, K. M., et al. 2016, A&A, 585, 149
Yorke, H. W., & Bodenheimer, P. 1999, ApJ, 525, 330
Young, E. T., Herter, T. L., Güsten, R., et al. 2012, Proc. SPIE, 8444, 844410
Zapata, L. A., Fernandez-Lopez, M., Curiel, S., Patel, N., & Rodriguez, L. F. 2013, arXiv:1305.4084
Zapata, L. A., Rodríguez, L. F., & Kurtz, S. E. 2001, RMxAA, 37, 83
Zavagno, A., Lagage, P. O., & Cabrit, S. 1999, A&A, 344, 499
Zhang, B., Zheng, X. W., Reid, M. J., et al. 2009, ApJ, 693, 419
Zhang, Q., Hunter, T. R., Sridharan, T. K., & Cesaroni, R. 1999, ApJL, 527, L117
Zhang, Q., Qiu, K., Girart, J. M., et al. 2014a, ApJ, 792, 116
Zhang, Y., & Tan, J. C. 2011, ApJ, 733, 55
Zhang, Y., & Tan, J. C. 2015, ApJL, 802, L15
Zhang, Y., Tan, J. C., De Buizer, J. M., et al. 2013a, ApJ, 767, 58
Zhang, Y., Tan, J. C., & Hosokawa, T. 2014b, ApJ, 788, 166
Zhang, Y., Tan, J. C., & McKee, C. F. 2013b, ApJ, 766, 86